JOURNAL OF PETROLOGY

Journal of Petrology, 2020, Vol. 61, No. 10: egaa095
doi: 10.1093/petrology/egaa095
Advance Access Publication Date: 20 October 2020
Original Article

OXFORD

Sulphur Behaviour and Redox Conditions in Etnean Magmas during Magma Differentiation and Degassing

Emanuela Gennaro [1]*, Antonio Paonita[1], Giada Iacono-Marziano[2], Yves Moussallam[3], Michel Pichavant[2], Nial Peters[4] and Caroline Martel[2]

[1]Istituto Nazionale di Geofisica e Vulcanologia, Sezione di Palermo, Via Ugo La Malfa 153, Palermo, 90146, Italy; [2]Institut des Sciences de la Terre d'Orléans (ISTO) UMR 7327, Université d'Orléans–CNRS–BRGM, Campus Géosciences, 1A rue de la Férollerie, Orléans, 45071, Cedex 2 (France); [3]Lamont–Doherty Earth Observatory, Columbia University, 61 Route 9W, Palisades, NY 10964-1000, USA; [4]Department of Geography, University of Cambridge, Downing Place, 20 Downing Place, Cambridge CB2 3EN, UK

*Corresponding author. E-mail: emanuelagennaro@live.it

Received 15 November 2019; Accepted 14 September 2020

ABSTRACT

Sulphur behaviour and variations in redox conditions during magma differentiation and degassing in the Mt Etna (Italy) volcanic system have been explored by integrating the study of olivine-hosted melt inclusions (MIs) with an experimental survey of sulphur solubility in hydrous basaltic magmas. Sulphur solubility experiments were performed at conditions relevant to the Etnean plumbing system (1200 °C, 200 MPa and oxygen fugacity between NNO + 0·2 and NNO + 1·7, with NNO being the nickel–nickel oxide buffer), and their results confirm the important control of oxygen fugacity (fO_2) on S abundance in mafic magmas and on S partitioning between fluid and melt phases ($DS^{fluid/melt}$). The observed $DS^{fluid/melt}$ value increases from 51 ± 4 to 146 ± 6 when fO_2 decreases from NNO + 1·7 ± 0·5 to NNO + 0·3. Based on the calculated $DS^{fluid/melt}$ and a careful selection of previously published data, an empirical model is proposed for basaltic magmas to predict the variation of $DS^{fluid/melt}$ values with variations in P (25–300 MPa), T (1030–1200°C) and fO_2 (between NNO − 0·8 and NNO + 2·4). Olivine-hosted melt inclusions (Fo_{89-91}) from tephra of the prehistoric (4 ka BP) sub-plinian picritic eruption, named FS ('Fall Stratified'), have been investigated for their major element compositions, volatile contents and iron speciation (expressed as $Fe^{3+}/\sum Fe$ ratio). These primitive MIs present S content from 235 ± 77 to 3445 ± 168 ppm, and oxygen fugacity values, estimated from $Fe^{3+}/\sum Fe$ ratios, range from NNO + 0·7 ± 0·2 to NNO + 1·6 ± 0·2. Iron speciation has also been investigated in more evolved and volatile-poorer Etnean MIs. The only primitive melt inclusion from the Mt Spagnolo eruption (4–15 ka BP) presents a S content of 1515 ± 49 ppm and an estimated fO_2 of NNO + 1·4 ± 0·1. The more evolved MIs (from 2002–2003, 2006, 2008–2009 and 2013 eruptions) have S content lower than 500 ppm, and their $Fe^{3+}/\Sigma Fe$ ratios result in fO_2 between NNO − 0·9 ± 0·1 and NNO + 0·4 ± 0·1. Redox conditions and S behaviour in Etnean magmas during degassing and fractional crystallization were modelled coupling MELTS code with our empirical $DS^{fluid/melt}$ model. Starting from an FS-type magma composition and upon decrease of T and P, fractional crystallization of olivine, clinopyroxene, spinel and plagioclase causes a significant fO_2 decrease. The fO_2 reduction, in turn, causes a decrease in sulphur solubility and an increase in $DS^{fluid/melt}$, promoting S exsolution during magma ascent, which further enhances the reduction of fO_2. For the evolved MIs of 2002–2013 eruptions, magma differentiation may therefore have played a crucial role in decreasing redox conditions and favouring efficient S degassing. Differently, during the unusual FS eruption, only limited melt evolution is observed and S exsolution seems to have been triggered by a major pressure decrease accompanied by H_2O and CO_2 exsolution during fast magmatic ascent.

Key words: melt inclusions; Mt Etna; redox conditions; sulphur solubility experiments; XANES $Fe^{3+}/\Sigma Fe$

INTRODUCTION

Volatile components play a key role in volcanic systems, affecting magma evolution and degassing and therefore ascent dynamics (e.g. Wallace & Edmonds, 2011). H_2O and CO_2 are the most abundant volatile components in magmas, followed by S components (principally SO_2 and H_2S) and halogens (mainly Cl, F).

S components generally receive particular attention because of their significant impact on atmospheric chemistry (e.g. Wallace & Edmonds, 2011) and Earth's average temperature (e.g. Robock, 2000). Indeed, sulphur released in the stratosphere during explosive volcanic eruptions, mainly as SO_2 (Oppenheimer, 2003), forms sulphate aerosols, which may backscatter the incoming solar radiation, causing atmospheric cooling that may persist for months or years, as observed, for example, during and after the eruptions of Mt Pinatubo (1991, e.g. Guo *et al.*, 2004), Laki (1783–1784, e.g. Thordarson & Self, 2003), Tambora (1816, e.g. Cole-Dai *et al.*, 2009), Samalas (1257, e.g. Vidal *et al.*, 2016), and Krakatoa (1883, e.g. Robock, 2000, and references therein).

In magmatic systems, the behaviour of sulphur is complex as it is linked to a multiplicity of parameters such as melt and volatile phase compositions, pressure, temperature, and redox conditions. Several experimental investigations have focused on the solubility of sulphur in hydrous silicic melts (e.g. Carroll & Rutherford, 1985, 1987; Luhr, 1990; Carroll & Webster, 1994; Botcharnikov *et al.*, 2004; Clemente *et al.*, 2004; Webster & Botcharnikov, 2011; Binder *et al.*, 2018) and in hydrous basaltic melts (e.g. Luhr, 1990; Liu *et al.*, 2007; Moune *et al.*, 2009; Beermann *et al.*, 2011, 2015; Lesne *et al.*, 2015). These studies showed that sulphur solubility in silicate melts is influenced by melt composition and oxygen fugacity (fO_2). Melt polymerization is, for instance, an important parameter controlling the solubility of sulphur-bearing minerals (Masotta & Keppler, 2015) and the fluid–melt partitioning of sulphur (Masotta *et al.*, 2016). Moreover, for a fixed composition, a decrease of temperature and pressure leads to a decrease in S solubility (e.g. Beermann *et al.*, 2011, 2015; Lesne *et al.*, 2011*a*; Webster & Botcharnikov, 2011).

The principal difficulty in constraining S behaviour in hydrous basaltic melts and, particularly, sulphur partitioning between the fluid phase and the silicate melt, is to evaluate its speciation as a function of the redox conditions. Experimental determinations clearly show that (1) sulphur dissolves in the melt primarily as sulphide species (S^{2-}) under reduced redox conditions, and mainly as sulphate species (S^{6+}) in more oxidized redox conditions (e.g. Fincham *et al.*, 1954; Carroll & Rutherford, 1985, 1988), and (2) sulphate species are significantly more soluble than sulphide ones (e.g. Carroll & Rutherford, 1985, 1987; Luhr, 1990; Jugo *et al.*, 2005; Beermann *et al.*, 2011, 2015; Botcharnikov *et al.*, 2011). The transition from sulphide- to sulphate-dominated systems occurs over a narrow fO_2 interval, roughly from NNO − 0·5 to NNO + 1·5 (Wallace & Carmichael, 1994; Jugo *et al.*, 2005; Jugo, 2009), where NNO represents the nickel–nickel oxide buffer, which is calculated through the equilibrium expression of Frost (1991) and is about 0·6 log units above the fO_2 of the fayalite–magnetite–quartz (FMQ) buffer at the considered pressures and temperatures. Such redox conditions correspond to the fO_2 conditions prevailing in magmas from arcs (Parkinson & Arculus, 1999) back-arcs, island-arcs and oceanic islands (Ballhaus, 1993; Moussallam *et al.*, 2019).

Melt inclusions (MIs) represent a crucial tool to provide information on the compositions and S content of primitive magmas (e.g. Métrich & Clocchiatti, 1989; Kamenetsky & Clocchiatti, 1996; Métrich *et al.*, 2004; Spilliaert *et al.*, 2006*a*; Kamenetsky *et al.*, 2007; Collins *et al.*, 2009; Schiavi *et al.*, 2015; Corsaro & Métrich, 2016; Moretti *et al.*, 2018; Gennaro *et al.*, 2019; Salem *et al.*, 2019). Olivine-hosted MIs can be used to investigate the fO_2 of their source region and to evaluate the redox variations of magmas during ascent and differentiation (e.g. Cottrell & Kelley, 2011; Kelley & Cottrell, 2012; Moussallam *et al.*, 2014, 2016; Hartley *et al.*, 2017).

Mt Etna (Italy) was chosen as a case study, because of the association of S-rich basaltic magmas (up to >4000 ppm S, Moretti *et al.*, 2018; Gennaro *et al.*, 2019) and high SO_2 fluxes (50 000 t in 2014, D'Aleo *et al.*, 2016). The available estimations of the redox conditions of this magmatic system vary from NNO to NNO + 1·8: phase equilibrium experiments on hawaiitic compositions (Mt Maletto, 1983 and 1991–1993 eruptions; e.g. Trigila *et al.*, 1990; Armienti *et al.*, 1994; Métrich & Rutherford, 1998) suggest fO_2 of ∼NNO; Cr-spinel and Fe–Ti oxides compositions in primitive basaltic compositions (Mt Spagnolo and 2001 eruptions; Kamenetsky & Clocchiatti, 1996; Kahl *et al.*, 2011) indicate fO_2 varying between NNO and NNO + 1·8; S speciation in melt inclusions (from 1989–1990, 2001, 'Fall Stratified' (FS) and Mt Spagnolo eruptions; Métrich & Clocchiatti, 1996; Métrich *et al.*, 2009; Morizet *et al.*, 2017) suggests fO_2 between NNO + 0·3 and NNO + 1.

To improve the knowledge of S behaviour and redox conditions of Etnean magmas during differentiation and degassing, we couple the study of natural olivine-hosted MIs with an experimental investigation of S solubility in Etnean hydrous alkali basalts.

We highlight how magma differentiation affects redox conditions and sulphur degassing of Etnean

magmas, explaining the variations from the most primitive MIs entrapped at depths >10 km below sea level (bsl) inside the plumbing system to the shallower and evolved MIs.

GEOLOGICAL BACKGROUND OF MT ETNA

Mt Etna is a basaltic, persistently active stratovolcano, situated on the boundary of the colliding African and European plates, close to the Aeolian subduction area (e.g. Clocchiatti *et al.*, 1998; Branca *et al.*, 2011). The activity started ~500 ka BP as a submarine volcano evolving toward an effusive–explosive aerial volcano. Subaerial activity of Mt Etna presents extremely variable styles, from effusive to highly explosive and caldera-forming (e.g. Branca *et al.*, 2011). The last stage of Etnean volcanism (recent Mongibello, 3–5 ka, Branca *et al.*, 2011) was marked by the alternation of lateral, eccentric or DDF ('Deep Dike Feed', Corsaro *et al.*, 2009) activity producing primitive magmas, and central and/or sub-terminal eruptions with the emission of more evolved magmas. Among the DDF eruptions, the most studied is the highly explosive (sub-plinian) Fall Stratified (FS) eruption, which occurred 4 ka BP (Coltelli *et al.*, 2005) and was characterized by an uncommon picritic magma.

By contrary, the majority of Etnean rocks have more evolved trachybasaltic compositions, and were erupted during either strombolian and paroxysmal activity at the summit craters (lava fountains and associated lava flows), or effusive to explosive flank eruptions, concurrently with the release of huge amounts of volatiles in the atmosphere (Aiuppa *et al.*, 2008). Indeed, Mt Etna is an important emitter of volatiles in the atmosphere, with an estimated average total flux of ~21 000 t day^{-1} during the 2005–2006 eruptive period (Aiuppa *et al.*, 2008). Among the major volatile species (H_2O, CO_2, S species), SO_2 is probably the most accurately measured in the Etnean plume (McGonigle *et al.*, 2003; Aiuppa *et al.*, 2005, 2008; Salerno *et al.*, 2009; D'Aleo *et al.*, 2016; Delle Donne *et al.*, 2019). D'Aleo *et al.* (2016) estimated up to ~50 000 t of SO_2 during the 2014 eruption, and important SO_2 fluxes are observed also during non-eruptive periods (~3563 t day^{-1}; Salerno *et al.*, 2009). However, these high SO_2 emissions are not fully constrained in terms of S origin and S behaviour during magma ascent and evolution.

Also strongly debated is the geochemical variability (e.g. increase of alkali, mainly K_2O, and radiogenic elements) in the recent Etnean magmas, as observed from isotopic and elemental geochemical data on rocks and melt inclusions (e.g. Correale *et al.*, 2014; Schiavi *et al.*, 2015; Corsaro & Métrich, 2016; Di Renzo *et al.*, 2019; Gennaro *et al.*, 2019; and references therein). For example, the post-1971 enrichment in alkalis (K, Rb, Cs) and radiogenic Sr and B elements (e.g. Armienti *et al.*, 2004; Métrich *et al.*, 2004; Allard *et al.*, 2006; Ferlito & Lanzafame, 2010) has been ascribed alternatively to (1) the interaction between an ocean island basalt (OIB) type (or HIMU-type) mantle source and an enriched component (EM1), corresponding to a slab-modified mantle or to (2) the mixing between mantle-derived magmas and a K- and Si-enriched melt (Schiano & Clocchiatti, 1994). On the other hand, Gennaro *et al.* (2019) proposed that part of the variability of major elements and volatiles observed in the Etnean magmas of the last 15 kyr could be ascribed to differentiation processes of a primitive FS-type magma, occasionally accompanied by secondary source-related and/or crustal processes.

SAMPLES AND METHODS

Etnean melt inclusions

Eleven olivine-hosted MIs from tephra of the FS subplinian DDF eruption were characterized for their chemical compositions and volatile contents, as well as Fe speciation.

FS tephra spreads mostly on the east and north flanks of the Etnean volcano, reaching a maximum thickness of 110 cm 7 km away from the summit craters. This rock (phenocrysts ≤10 vol%) has a picro-basaltic composition (MgO 17 wt%, Gennaro *et al.*, 2019), and contains euhedral $Fo_{89–91}$ olivine (up to ~5 mm in size), subhedral clinopyroxene and rare Cr-spinel, as microphenocrysts and/or included in olivine (e.g. Kamenetsky *et al.*, 2007; Correale *et al.*, 2014; Corsaro & Métrich, 2016; Gennaro *et al.*, 2019).

The MIs from FS products have already been characterized for their chemical compositions and volatile contents (Kamenetsky *et al.*, 2007; Corsaro & Métrich, 2016; Gennaro *et al.*, 2019). They are highly primitive (up to 12 wt% MgO) and show particularly high volatile contents, with H_2O up to 6 wt%, CO_2 up to >5000 ppm, S up to 3550 ppm, and Cl up to >3000 ppm. Entrapment depths calculated from H_2O and CO_2 contents range between 2 and 16 km bsl (Gennaro *et al.*, 2019), indicating that FS MIs are probably the most representative samples of the redox state of deep and primitive magmas.

To constrain the redox state of shallower and more evolved magmas, some olivine-hosted MIs from Mt Spagnolo (~4–15 ka BP), 2002–2003, 2006, 2008 and 2013 eruptions, previously analysed by Gennaro *et al.* (2019), have been also investigated by XANES spectroscopy. Unfortunately, only few MIs were analysable: one MI from Mt Spagnolo lava, two from 2002–2003 tephra, one from 2006 tephra, two from 2008–2009 tephra, and three from 2013 lavas, the last emitted during a paroxysmal event that contributed to produce the new South-East crater.

Mt Spagnolo lavas, produced by a DDF eruption, are located about 6 km NW of the central crater. Mt Spagnolo products present primitive characteristics; that is, high CaO/Al_2O_3 up to unity, olivine with $Fo_{74–89}$, presence of Cr-spinel, and high Sr content and $^{87}Sr/^{86}Sr$ ratios (e.g. Armienti *et al.*, 1988; Kamenetsky & Clocchiatti, 1996; Correale *et al.*, 2014; Gennaro *et al.*, 2019).

Table 1: Chemical composition of Mt Spagnolo anhydrous starting glass

oxide	wt%	±*
SiO_2	48·91	0·38
TiO_2	1·44	0·13
Al_2O_3	14·09	0·39
FeO	9·30	0·40
MnO	0·17	0·10
MgO	9·29	0·57
CaO	11·61	0·15
Na_2O	3·36	0·20
K_2O	1·27	0·10
P_2O_5	0·60	0·13
Total	100·03	0·67

Oxides composition obtained by electron microprobe (EMP) analysis. 'FeO' is the total iron as FeO.
*Standard deviation (1σ) calculated from 149 analysed points on two chips of the starting glass prepared in the same way (see main text for details) on two different days.

The 2002–2003 eruption was a DDF eruption, occurring along both the south and the north rift (eastward to the central craters), producing rocks with basaltic (around south rift) to evolved trachybasalt composition (e.g. Spilliaert *et al.*, 2006*a*, 2006*b*). The MIs investigated for Fe speciation are from tephra sampled along the south rift (and thus named '2002S', Gennaro *et al.*, 2019). The other investigated MIs are from tephra produced during the eruptions of 2006 (sub-terminal activity near the South-East crater), from bombs produced during intense explosions that occurred in the North-East crater in 2008–2009, and from lava emitted during a paroxysm that occurred at the New South-East crater in 2013 (Gennaro *et al.*, 2019). These trachybasalts have more evolved compositions with respect of 2002S and all Mt Spagnolo and FS rocks (e.g. Gennaro *et al.*, 2019).

Experimental methods

The starting material was prepared from the Mt Spagnolo lava, which is one of the most primitive basalts known to have erupted at Mt Etna (e.g. Kamenetsky & Clocchiatti, 1996; Correale *et al.*, 2014; Gennaro *et al.*, 2019). The rock was finely ground, melted in a Pt crucible at 1400 °C and 1 atm for 3 h, and rapidly quenched to produce a degassed crystal- and bubble-free starting glass (composition given in Table 1).

The experiments were carried out in a vertically operating internally heated pressure vessel (IHPV) at the Institut des Sciences de la Terre d'Orléans (ISTO, France). Platinum capsules (2·5 mm inner diameter, 0·2 mm wall thickness, 20 mm length) were used as containers. Compared with other metals and alloys such as AuPd or Pd (Pichavant *et al.*, 2006; Lesne, 2008; Le Gall, 2015), Pt is preferred for experiments performed at temperatures higher than 1050 °C and is less reactive with sulphur. It forms Fe–Pt sulphides at the capsule rim that generally lower the Fe content of the melts during experiment. We compensated for iron loss to the Pt capsule by adding variable amounts of FeO (0–6 wt%; Table 2) to the starting glass (Brugier *et al.*, 2015; Le Gall, 2015), while limiting the run duration as much as possible.

About 50 mg of powdered starting glass were loaded into Pt capsules, together with variable amounts of FeO, H_2O, S, and CO_2 (Table 2). Sulphur was added as elemental S (1–4 wt%, Table 2), and water as distilled H_2O. Both CO_2-free and CO_2-bearing charges (where CO_2 was added as dehydrated oxalic acid, $C_2H_2O_4.2H_2O$) were prepared, keeping the mass fraction of fluid component ($H_2O + CO_2$) to ∼10 % of the total mass of the charge (i.e. including volatiles, glass and sulphur, Table 2).

For each experimental run, up to four capsules were placed in the hotspot of the molybdenum furnace, and their temperature (T) was monitored with two S-type thermocouples (uncertainty ±5 °C) placed at the top and the bottom of the capsules. The T gradient along the capsules was always less than 10 °C. Ar was used as pressurizing medium and was mixed with variable amounts of H_2 to vary the fO_2. Total pressure was recorded by a transducer calibrated against a Heise Bourdon tube gauge with an uncertainty of ±20 bar. The experiments were performed at 1200 °C and between 180 and 210 MPa, and lasted between 2 and 3 h, to ensure the attainment of equilibrium between the basaltic melt and the fluid phase (e.g. Jugo *et al.*, 2005). This duration is sufficient to ensure homogeneous sulphur content in the silicate melts at the investigated temperature. Longer durations were found to corrode the Pt capsule and pierce it (Le Gall, 2015). All experiments were ended by a drop quench (estimated cooling rate of about 100 °C s^{-1}; Di Carlo *et al.*, 2006).

The aim of this experimental investigation was to confirm the effect of fO_2 on S behaviour at conditions relevant to those of the Etnean magmatic system in terms of volatile and FeO contents.

Redox conditions in each capsule were monitored using the solid sensor method, consisting of two pellets of metallic Co and Pd mixed with CoO (each pellet having a different starting Co_0/Pd_0 ratio), placed in a separate Pt capsule containing 15 wt% H_2O (Taylor *et al.*, 1992; Pownceby & O'Neill, 1994). Because CoPd may alloy with Pt, the redox-sensitive pellets were isolated from the capsule walls, by a sleeve of ZrO_2 powder. As Pt capsules are highly permeable to H_2 at elevated temperatures, the hydrogen fugacities of sensor and sample capsules are the same ($fH_{2(sensor)} = fH_{2(sample)}$; Taylor *et al.*, 1992). After experiment, analysis of CoPd ($X_{Co} = 0{\cdot}19 \pm 0{\cdot}05$, Table 2) alloys coexisting with CoO allows the fO_2 of the sensor to be determined (Pownceby & O'Neill, 1994). Then, $fH_{2(sensor)}$ and $fH_{2(sample)}$ are calculated from the water dissociation equilibrium equation $\log fH_2 = \log fH_2O - 1/2 \log fO_2 - \log K_w$, where K_w is the dissociation constant of water (calculated from Robie *et al.*, 1979) and fH_2O is the fugacity of pure H_2O at experimental P and T [calculated from Holloway (1987); see also Pichavant *et al.* (2014)].

Table 2: Experimental conditions, starting and product phases, and oxygen fugacity (log fO_2) values estimated using both the experimental sensors and the $Fe^{3+}/\Sigma Fe$ ratios evaluated by XANES

Exp. number	wt% FeO added	wt% S added	XH_2O	wt% H_2O added	wt% CO_2 added	experimental					XANES 2018			
						log fO_2*	ΔNNO	±	$Fe^{3+}/\sum Fe$	±	$Fe^{3+}/\sum Fe$	±	log fO_2	ΔNNO
SPA1702: T = *1200 ± 5° C*, P = *1802 ± 20 bars, time = 3 h*, X*Co = 0.22*														
SPA1702#1	0·00	0·90	1·00	9·95	—	–7·15	0·6	0·1	0·255	0·011	n.d.	—	n.d.	n.d.
SPA1702#2	1·79	0·89	1·00	10·53	—	–7·16	0·6	0·1	0·252	0·011	n.d.	—	n.d.	n.d.
SPA1702#3	2·69	0·90	1·00	10·33	—	–7·12	0·7	0·1	0·254	0·011	0·233	0·013	7·37	0·3
SPA1702#5	1·78	0·90	0·74	5·77	5·04	–7·45	0·3	0·1	0·231	0·011	0·226	0·013	–7·52	0·3
SPA2703: T = *1200 ± 5° C*, P = *2100 ± 20 bars, time = 3 h*, X*Co = 0.19*														
SPA2703#1	3·56	1·78	1·00	11·09	—	–6·76	1·0	0·1	0·284	0·013	0·222	0·013	–7·45	0·3
SPA2703#2	3·62	3·62	1·00	9·55	—	–6·81	0·9	0·1	0·283	0·013	0·275	0·013	–6·91	0·8
SPA2703#3	3·57	1·80	0·77	5·91	4·45	–7·17	0·5	0·1	0·247	0·012	n.d.	—	n.d.	n.d.
SPA2703#4	3·57	3·60	0·77	6·00	4·38	–7·13	0·6	0·1	0·253	0·012	n.d.	—	n.d.	n.d.
SPA2704: T = *1200 ± 5° C*, P = *1930 ± 20 bars, time = 3 h;* X*Co = 0.23*														
SPA2704#1	4·52	1·78	1·00	9·63	—	–7·13	0·6	0·1	0·255	0·011	n.d.	—	n.d.	n.d.
SPA2704#2	5·46	1·79	1·00	8·92	—	–7·12	0·6	0·1	0·250	0·011	0·221	0·013	7·47	0·2
SPA2704#3	4·54	3·50	1·00	9·24	—	–7·15	0·6	0·1	0·252	0·011	n.d.	—	n.d.	n.d.
SPA2704#4	4·43	3·63	0·73	5·75	5·22	–7·51	0·2	0·1	0·228	0·010	0·249	0·013	–7·25	0·5
SPA2704: T = *1200 ± 5° C, P = 2003 ± 20 bars, time = 2 h*, X*Co = 0.12*														
SPA1902#1	3·55	1·78	1·00	11·18	—	–5·98	1·7	0·5	0·357	0·052	n.d.	—	n.d.	n.d.
SPA1902#2	3·55	3·55	1·00	11·31	—	–5·98	1·7	0·5	0·359	0·051	n.d.	—	n.d.	n.d.

XH_2O is the molar fraction of H_2O loaded in the initial fluid phase [$XH_2O = (\text{mol } H_2O)/(\text{mol } H_2O + \text{mol } CO_2) = 1 - XCO_2$]. Log fO_2 (in bars) is expressed as ΔNNO (the log deviation from log fO_2 of the nickel–nickel oxide oxygen buffer reaction). The relative $Fe^{3+}/\Sigma Fe$ ratio values are calculated using the Kress & Carmichael (1991) method [equation (2)]. Using an inverse approach, the $Fe^{3+}/\Sigma Fe$ ratios, obtained from XANES methods, have been elaborated to obtain the relative log fO_2. All experimental products present an Fe–Pt–S reaction rim in the internal capsule wall. n.d., not determined.

*Experimental log fO_2 values are calculated from the XCo of the 'sensor' method as described in the main text. The XCO is calculated for each series of experimental runs, and those reported in the table are average values (the standard deviation is 0·03 for about 15 analysis of each CoPd alloy, and has been neglected for the followed fO_2 calculation).

For a given experimental run (constant P–T–fH_2), the fO_2 within each capsule varies along with its H_2O fugacity (fH_2O), which was determined for each charge from the H_2O content of the quenched glass, using the thermodynamic model for H_2O solution in multicomponent melts of Burnham (1979). Then, the fO_2 in each charge is calculated from the water dissociation equilibrium equation above. Results of the fO_2 calculations are given in Table 2. Typical uncertainties on log fO_2 range between 0·12 and 0·47 log units, propagated from an uncertainty of ±0·5 bar absolute on P_{H_2} (P_{H_2} is the pressure of H_2 gas initially loaded in the vessel at room temperature). The uncertainty on fO_2 therefore increases with decreasing P_{H_2}, being higher for the oxidized (lowest P_{H_2}) than for the reduced redox conditions (highest P_{H_2}) experiments.

Calculation of volatile contents in the fluid phase and S fluid/melt partitioning coefficients

The amount of sulphur (and other volatiles) contained in the fluid phase of the experimental capsules was estimated following the procedure described by Beermann *et al.* (2015). First, (1) the mass of the *i*th volatile species in the melt phase (mi_{melt}) was determined, to (2) calculate the respective mass in the fluid phase (mi_{fluid}):

$$mi_{melt} = ci_{melt} \times m_{glass}/100 - \Sigma c\mathrm{vol}_{melt}$$

$$mi_{fluid} = mi_{bulk} - mi_{melt}$$

where m_{glass} is the initial starting material mass, ci_{melt} (wt%) is the concentration of each volatile ($S + H_2O \pm CO_2$) dissolved in the melt phase (details on the estimation of volatiles in melt are given in the following section), $\Sigma c\mathrm{vol}_{melt}$ (wt%) is the total sum of volatile components dissolved in melt, and mi_{bulk} is the initial added quantity of each (*i*) volatile species.

Finally, the S concentration (cS_{fluid}, wt%) in the fluid phase was determined as follows:

$$cS_{fluid} = (mS_{fluid} \times 100)/\Sigma m\mathrm{vol}_{fluid}$$

where $\Sigma m\mathrm{vol}_{fluid}$ is the sum of the calculated mass of volatiles in the fluid phase and mS_{fluid} is the mass of S in the fluid phase as calculated before. Therefore, $DS^{fluid/melt}$ ($= S_{fluid}/S_{melt}$; concentration in wt%) is calculated using the amount of sulphur dissolved in the experimental glasses (S_{melt}) and the calculated sulphur exsolved in the fluid phase (S_{fluid}). Errors associated with the amount of S_{fluid} and the value of $DS^{fluid/melt}$ have also been estimated by using the calculation proposed by Beermann *et al.* (2015).

Analytical methods

Melt inclusions in olivine crystals and experimental products, mounted in epoxy resin, were imaged with two scanning electron microscopes (SEM): a Tescan MIRA 3 XMU (BRGM, Orléans), using 25 kV electron energy, and a Zeiss Merlin Compact (ISTO, Orléans), using 15 kV electron energy. Semi-qualitative analyses of sulphide droplets were also performed with these SEM devices.

Major elements, S and Cl concentrations in melt inclusions, olivine phenocrysts and experimental glasses were determined with a Cameca SX FIVE electron microprobe (EMP, at ISTO, Orléans) operated under an acceleration voltage of 15 kV, a beam current of 6 nA and a peak counting time of 10 s for all elements, except S (60 s). The metallic alloys of the sensors were analysed with an acceleration voltage of 20 kV and a beam current of 20 nA. The Pt capsule walls were also analysed for their Fe and S contents, using an acceleration voltage of 20 kV and 30 nA beam current. A focused beam was used for olivine and metals, whereas beams of 2–6 and 6–12 μm were used respectively for melt inclusions and experimental glasses, to reduce Na migration. Natural minerals and oxides were used as standards (albite for Na and Si; anorthoclase for K; anhydrite for Ca; apatite for P; vanadinite for Cl; MgO for Mg; Al_2O_3 for Al; Fe_2O_3 for Fe; $MnTiO_3$ for Ti and Mn; metal Pt for Pt); S was calibrated against barite ($BaSO_4$).

H_2O and CO_2 contents in the glass phase of the FS doubly polished MIs were determined by Fourier transform infrared spectroscopy (FTIR) using a Nicolet 6700 Magna spectrometer equipped with an IR microscope and an MCT detector (ISTO, Orléans). The thickness of each chip (27–56 μm) was assessed using a petrographic microscope, through repeated measurements. For each melt inclusion, at least two spectra were acquired to check the homogeneity of dissolved volatile contents. Absorption spectra were acquired in the range 1000–6000 cm^{-1} with 128/560 scans and a resolution of 4 cm^{-1}, using a Globar internal IR source and a KBr beam-splitter. The H_2O and CO_2 concentrations (C) were calculated respectively from the absorbance (A) of the 3530 cm^{-1} (total H_2O) and of the 1430 and 1525 cm^{-1} doublet (CO_3^{2-} bending) bands, using the modified Beer–Lambert law (Stolper, 1982):

$$C = [(\mathrm{MW} \times A)/(d \times l \times \varepsilon) \times 100]$$

where MW is the molecular weight (g mol^{-1}), d is the melt density (g l^{-1}), ε is the molar absorption coefficient (l mol^{-1} cm^{-1}), l is the optic path (i.e. the thickness of the glass sample, cm). A molar extinction coefficient (ε) of 63 l mol^{-1} cm^{-1} was used for the 3530 cm^{-1} band (Dixon *et al.*, 1988), whereas the coefficient for the 1525 cm^{-1} band (415 ± 4 l mol^{-1} cm^{-1}) was calculated for each MI on the basis of the Na/(Na + Ca) molar ratio of the melt, using the Dixon & Pan (1995) method.

The absorbance values of the carbonate doublet were estimated after subtraction of a spectrum of a CO_2-free synthetic glass with similar composition and H_2O content (Lesne *et al.*, 2011*b*). The density of natural glasses (2·70 ± 0·03 g cm^{-3}) was calculated from the density of the starting anhydrous basaltic experimental glass (2·78 g cm^{-3}, Gennaro, 2017). The effect of dissolved water was accounted for using the method of

Richet *et al.* (2000) and CO_2 was assumed to have no influence on the glass density (Bourgue & Richet, 2001).

For experimental glasses, H_2O and CO_2 contents were determined by secondary ion mass spectrometry (SIMS), using both a Cameca IMS 1270 and a Cameca IMS 1280 HR2 instrument (Centre de Recherches Pétrographiques et Géochimiques, Nancy, France). Experimental and standard glasses were pressed into indium within an aluminium disk, and then gold coated and outgassed in the SIMS chamber until a pressure of 10^{-8}–10^{-9} Torr was reached. The acquisition, preceded by a 30 s pre-sputtering period (to remove impurities from the sample surface), was performed using a Cs^+ primary beam of 5 nA, with an impact energy of 20 kV in 12–15 cycles. Glasses with compositions similar to the Etna samples including N72 basalt from Kamchatka and KL2-G basalt from Kilauea (H_2O = 0–4·2 wt% and CO_2 = 0–3172 ppm; Jochum *et al.*, 2006; Shishkina *et al.*, 2010) were used as standards. The signals for $^{12}C^-$ and $^{16}O^1H^-$ were gathered in monocollection mode during the same analysis (acquisition time of 12 min). Concentrations of CO_2 were calculated by comparing the $^{12}C^-/^{28}Si^-$ vs SiO_2 of the sample with that of the reference glass. H_2O was calculated by comparing the OH^-/H^- vs H_2O in the reference materials with the obtained OH^-/H^- of the sample.

The H_2O and CO_2 of MIs from Gennaro *et al.* (2019) had been estimated by SIMS, following the same procedure as described above.

XANES Fe^{3+}/Fe investigation

The pre-edge structure of the Fe K-edge (Fig. A1 in Supplementary Data Electronic Appendix 1; supplementary data are available for downloading at http://www.petrology.oxfordjournals.org) was investigated in 21 double-polished MIs, one matrix glass and one embayment from this study (FS) and from Gennaro *et al.* (2019; FS, Mt Spagnolo, 2002–2013 eruptions) and in six experimental glasses by X-ray absorption near edge structure (XANES) at the Diamond Light Source (DLS, Oxfordshire), using the I18 beamline over the energy range 7020–7500 eV, to determine the $Fe^{3+}/\Sigma Fe$ ratio. During the analytical acquisition, the storage ring was operating at 3 GeV with an electron current of about 300 mA.

XANES spectra were acquired during two analytical sessions. In a first session (in 2015), seven MIs (from Mt Spagnolo, 2002–2003, 2006, 2008–2009, 2013 eruptions), one embayment (from 2006) and one matrix glass (2002–2003 eruption) from Gennaro *et al.* (2019) were analysed using methods described by Moussallam *et al.* (2014, 2016).

The X-rays were focused with Kirkpatrick–Baez mirrors down to 2 μm (horizontal) × 2·5 μm (vertical) beam size. The beamline utilizes a liquid nitrogen-cooled double-crystal monochromator with silicon crystals, and Si (333) reflection was used to increase the energy resolution. Measurements were performed in fluorescence mode, and the energy-dispersive detector used was a six-element SGX Sensortech silicon drift detector positioned at 90° with respect to the incident X-ray beam. The sample was positioned such that the normal to its surface was tilted 10° relative to the incident X-ray beam to improve the horizontal resolution and reduce potential self-absorption effects. The incident X-ray beam was filtered with Al foils (varying in thickness from 0·025 to 0·1 mm) with the aim of keeping the detector count rate within the linear response region and removing the effect of beam damage on the sample. The energy step sizes and dwell times used are given in Table A1 (Supplementary Data Electronic Appendix 1).

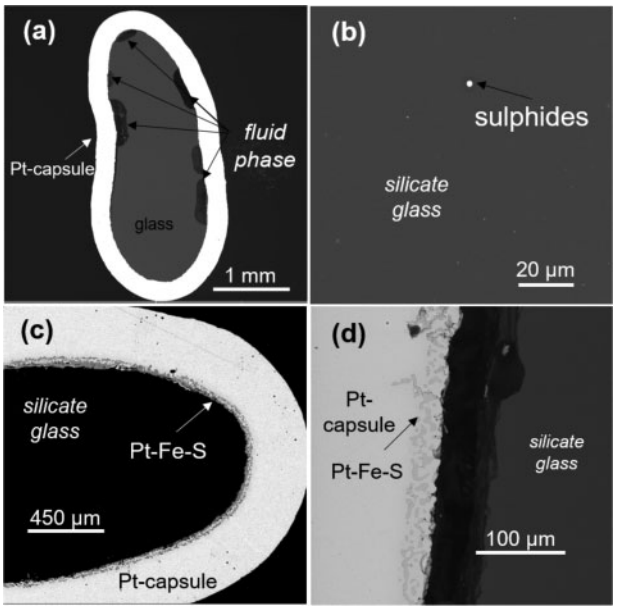

Fig. 1. Backscattered electron images of experimental products: (a) gas bubbles located at the glass–Pt-capsule interface (SPA2703#3); (b) glass (SPA2704#4) with small sulphide globules; (c, d) internal walls of Pt-capsules showing reaction rims (Pt–Fe–S).

In a second session (in 2018), XANES spectra were collected for the six experimental glasses and the 11 MIs from FS tephra characterized in this study, along with three MIs from Gennaro *et al.*, 2019 (one MI from each of the 2002–2003, 2013 and FS eruptions) following the methods described by Moussallam *et al.* (2019). The X-rays were focused with Kirkpatrick–Baez mirrors down to 2 μm (horizontal) × 1·2 μm (vertical) beam size. Measurements were performed in fluorescence mode using two energy-dispersive Vortex ME-4 silicon drift detectors positioned at 45° to the incident beam (one located directly above the other and pointing towards the sample). The sample was positioned so that the normal to the sample surface was at 45° to the incident X-ray beam. The incident X-ray beam was filtered with an Al foil of 0·25 mm thickness to remove the effect of beam damage on the sample (see Supplementary Data Electronic Appendix 1). The energy step sizes and dwell times used during the 2018 session are the same as those used for the 2015 acquisition (Table A1 in

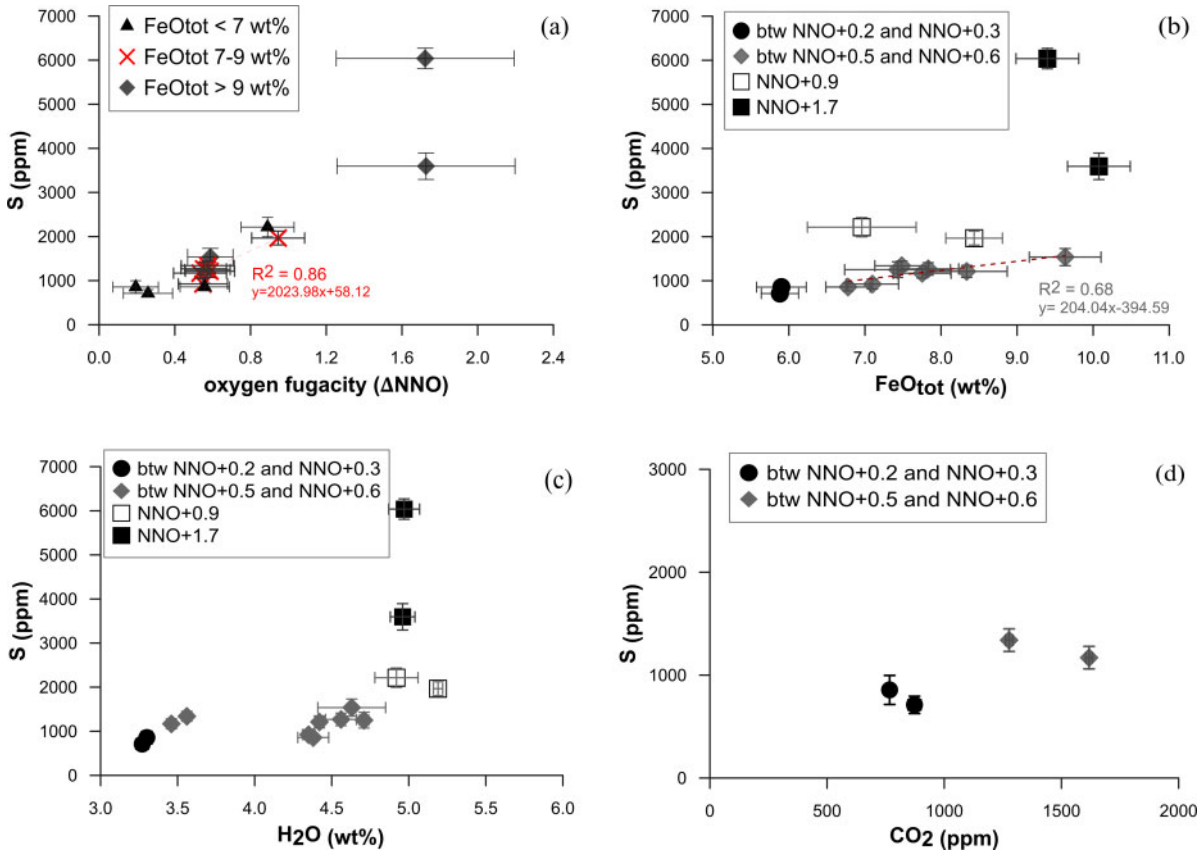

Fig. 2. S content of experimental glasses as function of (a) oxygen fugacity (reported in bar and expressed as ΔNNO; i.e. log unit deviation from log fO_2 of the nickel–nickel oxide oxygen buffer reaction), (b) glass FeO_{tot} content, (c) glass H_2O content and (d) glass CO_2 content. FeO_{tot} concentrations are normalized on a volatile-free basis. The error bars indicate the standard deviation (1σ). "btw" = between.

Supplementary Data Electronic Appendix 1). For the MIs, two spectra were acquired and co-added for each analysis.

In total, during the two sessions, 52 MIs were exposed to the XANES beam, but many spectra exhibited olivine contamination (Fig. A2, Supplementary Data Electronic Appendix 1) and other analytical problems, and thus were not further considered.

The NMNH 117393 dry basalt glasses, loaned by the Smithsonian Institution National Museum of Natural History, were used as reference and their spectra were acquired under the same conditions as applied to the investigated samples during both sessions. Their $Fe^{3+}/\Sigma Fe$ ratios have been measured by Mössbauer spectroscopy (Cottrell *et al.*, 2009; Zhang *et al.*, 2018). The reference glasses were analysed at the beginning and end of each session and an average spectrum for each glass was used to derive the calibration curve (see Supplementary Data Electronic Appendix 1 for details on calibration and data processing).

RESULTS

Experimental charges

Experimental products are brown, uniformly coloured and crystal-free glasses (Fig. 1a), except for the presence of small sulphide globules (<3 μm in diameter, Fig. 1b) in the most reduced runs (fO_2 < NNO + 1). Their size did not allow EMP analysis, but semi-qualitative SEM–energy-dispersive spectra indicate that they are mainly constituted of Fe, Pt and S. Rare microbubbles are observed in the melt, whereas larger bubbles are frequently located at the glass–capsule interface (Fig. 1a), indicating fluid saturation. The presence of a free fluid phase in each experimental capsule was corroborated by the weight loss after piercing the capsules at the end of the experiment.

The internal walls of all Pt-capsules present a rim of Pt–Fe–S aggregates, which range in thickness from ~10 to 80 μm. SEM imaging (Fig. 1c and d) shows that, for a given run, the thickest reaction rims are for the charges with CO_2 and in which the highest amounts of S were added.

Major element compositions and volatile contents

Major element compositions and volatile contents of the 14 basaltic experimental glasses are reported in Table 3. Measured standard deviations for major elements are generally low (Table 3), indicating homogeneous compositions.

Dissolved H_2O contents range from 3·3 to 5·2 wt% (Table 3) with the lowest concentrations (<4 wt%) in the CO_2-bearing glasses (SPA 1702#5, 2703#3, 2703#4, 2704#4), which contain between 767 and 1618 ppm CO_2. The dispersion in the H_2O and CO_2 measurements is very low (0·02–0·22 wt% and 8–27 ppm, respectively), signifying that the experimental glasses contain homogeneous concentrations of dissolved H_2O and CO_2.

The sulphur content of the experimental glasses varies from 711 to 6039 ppm, with standard deviations between 84 and 300 ppm (Table 3). The only two parameters that were varied in our experimental runs (Table 2) and that affect the S content of the silicate melt are FeO_{tot} and fO_2 (e.g. Jugo *et al.*, 2005; Zajacz *et al.*, 2012; Lesne *et al.*, 2015). Considering experimental glasses with similar FeO_{tot} content, oxygen fugacity is confirmed to be the main parameter affecting sulphur solubility in our experiments (Fig. 2a), in agreement with previous studies (e.g. Jugo *et al.*, 2005, and references therein). We cannot evaluate the effect of melt composition on the S content of our glasses, given the extremely low variability of major element compositions. Only the FeO_{tot} content varies from 5·9 to 10·1 wt% (Table 3), but no clear correlation with the S content is observed (Fig. 2b), most probably owing to the effect of fO_2. When considering samples within a narrow range of fO_2 (between NNO + 0·5 and NNO + 0·6), a slight positive correlation between S and FeO_{tot} contents can be noted (Fig. 2b).

No clear relationship is observed between the S and the H_2O contents of our experimental glasses (Fig. 2c), or between S and CO_2 contents (Fig. 2d), probably because of the more important effect of fO_2. Previous studies have proposed either a positive (e.g. Moune *et al.*, 2009; Fortin *et al.*, 2015) or a negative effect (Liu *et al.*, 2007; Li & Ripley, 2009) of the water content on the sulphur content at sulphide saturation (SCSS). Moretti & Baker (2008) suggest that the effect of water on SCSS can be variable, depending on pressure and melt compositions. We do not participate in this debate, given that our experiments show that the effect of fO_2 largely overwhelms the effects of FeO and H_2O contents on SCSS. To model the behaviour of S during ascent and crystallization of Etnean magmas, we will therefore point out the effect of fO_2 and neglect those of melt composition, including H_2O content.

Fluid/melt partitioning of sulphur

The amount of sulphur dissolved in the melt (S_{melt}, in wt%, Table 3) and that calculated in the fluid phase of the experiments (S_{fluid}, in wt%, Table 3 and in Fig. S1 in Supplementary Data Electronic Appendix 2) are used for calculating the S fluid/melt partitioning coefficient ($DS^{fluid/melt} = S_{fluid}/S_{melt}$; Table 3). The presence of sulphide globules and the Pt–Fe–S alloy at the internal capsules walls is neglected in the calculation of the S_{fluid}, as in previous studies (e.g. Beermann *et al.*, 2015; Le Gall, 2015; Lesne *et al.*, 2015), because of the difficulty of evaluating their abundances. Calculated $DS^{fluid/melt}$ values are therefore maximal values, because S contained in these phases is implicitly included in S_{fluid}. Because of this problem, the values of $DS^{fluid/melt}$ calculated for samples showing thick Pt–Fe–S aggregates at the capsule rim were not selected for our modelling. We used the approach described by Alletti *et al.* (2009) to refine this selection and check whether the calculated $DS^{fluid/melt}$ values unequivocally indicate the partition of S between the fluid and melt phases or if they are strongly perturbed by S loss in the sulphide phase (Fe–Pt–S globules in melt) and/or at the capsule wall. In a plot S_{melt} versus S_{fluid} (Fig. S1a in Supplementary Data Electronic Appendix 2) it is observed that for glasses with dissolved S_{melt} <2500 ppm, the calculated S_{fluid} increases strongly (from 10 to 40 wt%), whereas S_{melt} is almost constant (0·1–0·2 wt%), indicating that in these runs an additional S-bearing phase sequesters a significant part of S of the system (Alletti *et al.*, 2009, and references therein).

The selected $DS^{fluid/melt}$ values range between 50 ± 4 and 146 ± 6 (Fig. 3, Table 3) and are within the range of previous experimental estimates on Etna trachybasalts (1–236, Beermann *et al.*, 2015) and on other basalt compositions (7–2814, Lesne *et al.*, 2011*a*; Zajacz *et al.*, 2013; Fiege *et al.*, 2015; Le Gall, 2015).

Because our experimental *P*–*T* conditions and melt composition are constant, the only parameter affecting $DS^{fluid/melt}$ is fO_2. Among the selected values, $DS^{fluid/melt}$ decreases with increasing fO_2 (Fig. 3, red cross-shaped symbols), with the lowest $DS^{fluid/melt}$ value (50 ± 4) corresponding to the samples with the most oxidized redox conditions (fO_2 = NNO + 1·7 ± 0·5). Previous studies also suggest the influence of pressure and temperature on $DS^{fluid/melt}$ (e.g. Lesne *et al.*, 2011*a*; Webster & Botcharnikov, 2011). Pressure and $DS^{fluid/melt}$ are generally inversely correlated (Lesne *et al.*, 2011*a*). The relation with temperature remains unclear; only the decompression and annealing experiments of Fiege *et al.* (2015) show an inverse relation between $DS^{fluid/melt}$ and *T*, in the 1150–1250 °C range.

Considering our results and a selection of data previously published (Lesne *et al.*, 2011*a*; Zajacz *et al.*, 2013; Beermann *et al.*, 2015; Le Gall, 2015), we calibrated, for a basaltic magma, an empirical model for the dependence of $DS^{fluid/melt}$ on fO_2, *P*, and *T*:

$$\log(DS^{fluid/melt}) = a/T + bP + c\Delta\mathrm{NNO} + d \qquad (1)$$

where *T* is in °C, *P* is in MPa, *a* = –7621·011, *b* = –0·0016, *c* = –0·462 and *d* = 9·117 (Table S1 in Supplementary Data Electronic Appendix 2).

The selected dataset used for this model includes basaltic glasses quenched at *T* = 1030–1200 °C, *P* = 25–300 MPa, and $\log fO_2$ between NNO – 0·8 and NNO + 2·4, chosen with the same criterion as used for our data (as used by Alletti *et al.*, 2009). We used the data from Beermann *et al.* (2015), which have an Etnean composition, excluding (1) the glasses in which the

Table 3: Major element composition and volatile contents of the experimental glasses, and S fluid/melt partition coefficients*

Exp. number†	SiO_2	TiO_2	Al_2O_3	FeO_{tot}‡	MnO	MgO	CaO	Na_2O	K_2O	P_2O_5	Total	Fe loss (%)	S_{melt} (ppm)	H_2O	CO_2	S_{fluid} (wt%)	$DS^{fluid/melt}$
SPA1702#1 [15]	50·59 (±0·47)	1·49 (±0·10)	14·61 (±0·22)	6·78 (±0·29)	0·16 (±0·08)	9·31 (±0·13)	11·81 (±0·15)	3·38 (±0·09)	1·30 (±0·08)	0·57 (±0·12)	94	−27 (±3)	858 (±88)	4·38 (±0·10)		12·3 (±3·5)	143 (±4)
SPA1702#2 [30]	50·80 (±0·31)	1·50 (±0·12)	14·65 (±0·19)	7·10 (±0·35)	0·18 (±0·10)	9·02 (±0·12)	11·72 (±0·13)	1·28 (±0·07)	3·25 (±0·08)	0·50 (±0·13)	93	−24 (±4)	925 (±112)	4·35 (±0·04)		11·1 (±3·0)	120 (±3)
SPA1702#3 [30]	49·90 (±0·40)	1·44 (±0·12)	14·31 (±0·17)	8·34 (±0·53)	0·15 (±0·08)	9·07 (±0·09)	11·58 (±0·12)	3·35 (±0·07)	1·30 (±0·07)	0·57 (±0·11)	94	−10 (±6)	1212 (±136)	4·42 (±0·03)		11·2 (±3·4)	92 (±4)
SPA1702#5 [15]	51·88 (±0·38)	1·55 (±0·11)	14·61 (±0·22)	5·88 (±0·24)	0·17 (±0·09)	8·89 (±0·06)	12·02 (±0·08)	1·32 (±0·08)	3·20 (±0·08)	0·48 (±0·13)	94	−37 (±3)	711 (±84)	3·27 (±0·04)	873 (±27)	10·3 (±6·3)	146 (±6)
SPA2703#1 [95]	49·72 (±0·54)	1·48 (±0·12)	14·28 (±0·20)	8·44 (±0·37)	0·15 (±0·11)	9·14 (±0·11)	11·64 (±0·16)	3·26 (±0·10)	1·30 (±0·09)	0·61 (±0·11)	92	−9 (±4)	1966 (±156)	5·19 (±0·03)		20·2 (±3·3)	103 (±3)
SPA2703#2 [45]	50·57 (±0·41)	1·45 (±0·09)	14·52 (±0·21)	6·96 (±0·71)	0·14 (±0·07)	9·31 (±0·11)	11·85 (±0·11)	3·30 (±0·09)	1·30 (±0·09)	0·59 (±0·13)	93	−25 (±8)	2215 (±219)	4·92 (±0·14)		40·4 (±10·3)	182 (±10)§
SPA2703#3 [110]	49·73 (±0·55)	1·45 (±0·12)	14·67 (±0·35)	7·75 (±0·38)	0·17 (±0·09)	9·30 (±0·13)	11·68 (±0·20)	3·34 (±0·08)	1·31 (±0·07)	0·60 (±0·13)	94	−17 (±4)	1170 (±109)	3·46 (±0·03)	1618 (±14)	20·5 (±6·5)	175 (±7)§
SPA2703#4 [115]	50·12 (±0·90)	1·44 (±0·10)	14·52 (±0·30)	7·48 (±0·35)	0·18 (±0·09)	9·26 (±0·11)	11·77 (±0·24)	3·34 (±0·08)	1·31 (±0·08)	0·58 (±0·13)	93	−20 (±4)	1340 (±110)	3·56 (±0·03)	1277 (±16)	34·42 (±13·6)	257 (±14)§
SPA2704#1 [39]	50·17 (±0·47)	1·45 (±0·09)	14·54 (±0·25)	7·43 (±0·70)	0·15 (±0·09)	9·22 (±0·15)	11·72 (±0·15)	3·46 (±0·08)	1·26 (±0·08)	0·61 (±0·14)	94	−20 (±7)	1252 (±179)	4·71 (±0·03)		24·4 (±11·1)	195 (±116)§
SPA2704#2 [45]	48·99 (±0·45)	1·40 (±0·09)	14·07 (±0·20)	9·63 (±0·47)	0·16 (±0·07)	9·12 (±0·10)	11·33 (±0·14)	3·42 (±0·08)	1·27 (±0·09)	0·61 (±0·14)	93	4 (±5)	1537 (±194)	4·63 (±0·22)		26·8 (±6·9)	175 (±7)§
SPA2704#3 [68]	49·96 (±0·32)	1·46 (±0·12)	14·37 (±0·19)	7·83 (±0·40)	0·17 (±0·09)	9·26 (±0·09)	11·60 (±0·14)	3·47 (±0·08)	1·29 (±0·08)	0·58 (±0·14)	94	−16 (±4)	1269 (±142)	4·56 (±0·10)		40·9 (±11·5)	323 (±12)§
SPA2704#4 [74]	50·94 (±0·54)	1·49 (±0·10)	14·84 (±0·21)	5·90 (±0·33)	0·17 (±0·09)	9·48 (±0·14)	11·66 (±0·15)	3·63 (±0·20)	1·33 (±0·09)	0·57 (±0·14)	94	−37 (±3)	856 (±141)	3·30 (±0·02)	767 (±8)	32·1 (±15·0)	375 (±15)§
SPA1902#1 [45]	49·44 (±0·38)	1·41 (±0·13)	14·00 (±0·17)	10·08 (±0·41)	0·16 (±0·04)	9·08 (±0·11)	11·36 (±0·11)	3·22 (±0·10)	1·26 (±0·09)	n.d.	93	8 (±4)	3595 (±30)	4·96 (±0·08)		17·9 (±3·6)	50 (±4)
SPA1902#2 [33]	49·93 (±0·38)	1·41 (±0·13)	14·11 (±0·17)	9·40 (±0·41)	0·16 (±0·04)	9·07 (±0·11)	11·39 (±0·11)	3·26 (±0·10)	1·27 (±0·09)	n.d.	92	1 (±4)	6039 (±232)	4·97 (±0·10)		30·6 (±3·5)	51 (±4)

All oxides (expressed in wt%) and S_{melt} (ppm = $\mu g\,g^{-1}$) contents are from EMP analysis. H_2O (wt%) and CO_2 (ppm) are from SIMS analysis. Major element concentrations are normalized to 100 % on a volatile-free basis. $DS^{fluid/melt} = S_{fluid}$ (wt%)/S_{melt} (wt%), where S in the fluid (S_{fluid}, wt%) is calculated following the procedure of Beermann *et al.* (2015), as described in the main text. Fe loss calculated as $100(FeO_{exp} - FeO_{start})/(FeO_{start})$ where FeO_{exp} and FeO_{start} are from this table (= FeO_{tot}) and Table 1, respectively, after normalization to 100 % on volatile-free basis. n.d., not determined.

*Numbers in parentheses are the standard deviations (1σ).

†The number in square brackets (in the first column) indicates the number of EMP analyses. Standard deviations (1σ) for H_2O and CO_2 concentrations are calculated on five repeated analyses for each glass.

‡FeO_{tot} is the total iron as FeO. Total is the total sum of major oxides as obtained by EMP before the normalization to 100 wt%.

§These $DS^{fluid/melt}$ values are not used in the discussion or in the regression model decribed in the main text because they are probably significantly affected by the presence of sulphide globules (see main text and Supplementary Data for details).

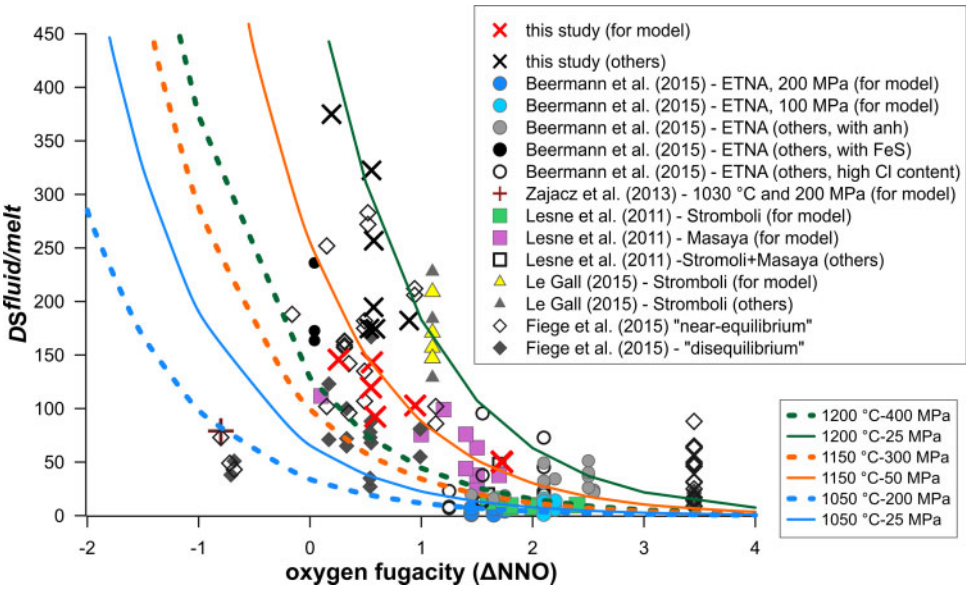

Fig. 3. $DS^{fluid/melt}$ (calculated wt% S in fluid phase/wt% S in basaltic melt) determined in this study, together with literature data (Lesne *et al.*, 2011*a*; Zajacz *et al.*, 2013; Beermann *et al.*, 2015; Fiege *et al.*, 2015; Le Gall, 2015). The data used to calibrate the empirical model described in the text are labelled 'for model', whereas those that were not used are labelled 'others'. Decompression and annealing experimental data of Fiege *et al.* (2015) not used in the model are also shown in the plot. In the plot, the coloured curves show the dependence of $DS^{fluid/melt}$ on fO_2 predicted by the model [equation (1)] at variable *T*–*P* conditions.

presence of a S-bearing phase is important (those with anomalous correlation between S_{fluid} and S_{melt} concentration, as described above) and (2) those with unrealistically (for Etna) high Cl content.

We also considered the data of the decompression experiments from Le Gall (2015) and Lesne *et al.* (2011*a*), performed with Stromboli and Masaya basaltic compositions (selected with the approach as above). The data from the decompression (plus annealing) experiments of Fiege *et al.* (2015), also shown in Fig. 3, are excluded from our empirical $DS^{fluid/melt}$ model, because even those approaching near-equilibrium conditions show a negative correlation in the S_{fluid} vs S_{melt} concentration plot (not shown).

Figure 3 shows the selected values of $DS^{fluid/melt}$ used for the proposed empirical model. Our data highlight the relation between $DS^{fluid/melt}$ and fO_2 at constant *T* (1200 °C) and *P* (~200 MPa). The other data corroborate this relation despite the variability of *P* and *T* conditions. Figure 3 also shows the curves of $DS^{fluid/melt}$ versus fO_2 calculated by the model [equation (1)] at various *T*–*P* conditions. The model predicts that fO_2 and *T* more significantly affect $DS^{fluid/melt}$ values than *P* (Fig. 3). Notably, the effect of a decrease in both fO_2 and *P* is to increase $DS^{fluid/melt}$; this increase can be partially counterbalanced by a decrease of *T*.

Modelled $DS^{fluid/melt}$ as function of *T*, *P* and fO_2 gives a coefficient of determination (R^2) of 0·79 (Fig. S2 in Supplementary Data Electronic Appendix 2). The large uncertainty in the estimation of both the experimental fO_2 and the amount of S in the experimental fluid phase (mainly owing to the occurrence of sulphide phases), along with differences in the basaltic compositions and in the experimental setup prevents further improvement of this best fit.

$Fe^{3+}/\Sigma Fe$ ratio of the experimental glasses

The $Fe^{3+}/\Sigma Fe$ ratios of experimental glasses, measured by XANES, range from 0·22 to 0·27 (Table 2), with a precision (1σ) of 0·013. These values are generally lower than those calculated from the fO_2 imposed in the experiment (named 'experimental' in Table 2 and Fig. 4), using the empirical formulation of Kress & Carmichael (1991), which relates $Fe^{3+}/\Sigma Fe$ ratios to fO_2, accounting for the chemical composition of the silicate melt, pressure and temperature:

$$(XFe_2O_3/XFeO) = a\ln(fO_2) + b/T + c + \sum d_iX_i + e\,[1 - T_0/T - \ln(T/T_0)] + fP/T + g[(T - T_0)P]/T + h\,P^2/T \quad (2)$$

where *a*, *b*, *c*, *d*, *e*, *f*, *g* and *h* are constants, X_i are mole fractions of oxide components in silicate melts, *T* and *P* are in Kelvin and kbar, respectively, and T_0 is fixed to 1673 K.

However, the observed discrepancy (Fig. 4) is comparable with the typical uncertainty on experimental $Fe^{3+}/\Sigma Fe$ ratios, which varies between 0·010 and 0·052, with increasing redox conditions glasses (see 'Experimental methods' section).

Melt inclusions

Primitive melt inclusions from FS eruption

MIs, entrapped in $Fo_{90–91}$ olivine phenocrysts from the FS scoria, have spherical and oval shapes (48–225 μm size), with typical scalloped edges (Fig. 5a and b;

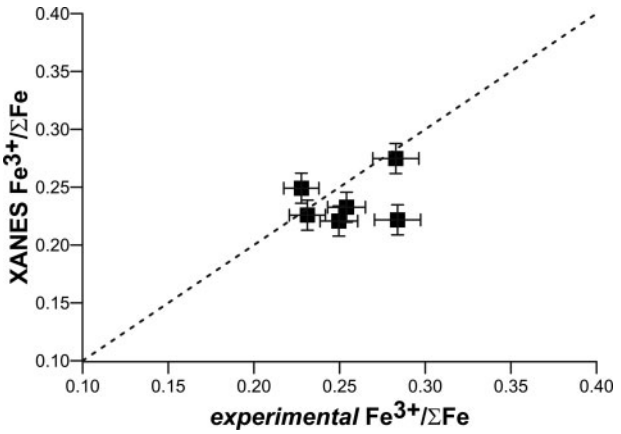

Fig. 4. $Fe^{3+}/\Sigma Fe$ ratios determined by XANES spectroscopy available for some experimental glasses, plotted against $Fe^{3+}/\Sigma Fe$ ratios calculated from experimental fO_2 using equation (2) (Kress & Carmichael, 1991). Precisions (1σ) of XANES measurements are 0·013. Uncertainties on experimental $Fe^{3+}/\Sigma Fe$ ratios (between 0·010 and 0·052) are propagated from uncertainties on experimental fO_2 (see main text).

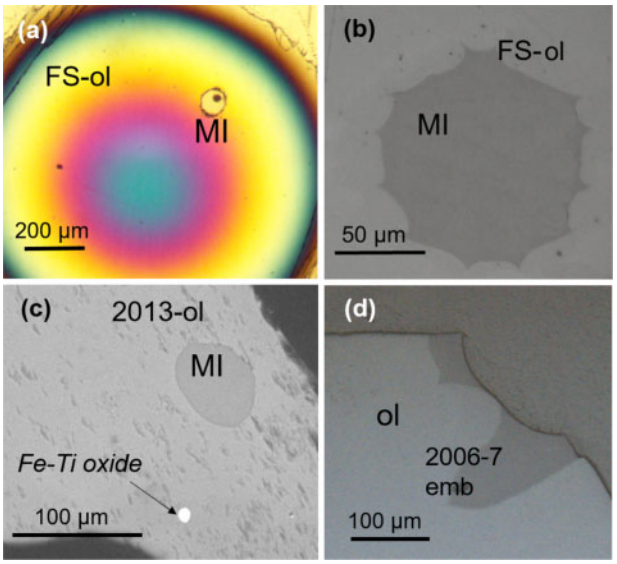

Fig. 5. (a) FS olivine crystal entrapping a bubble-bearing MI. (b) MI from FS tephra with typical scalloped edges. (c) Typical MI with circular shape in 2013 olivine. (d) Embayment surrounding the 2006–2007 olivine crystal.

Kamenetsky *et al.*, 2007). They consist of transparent glass, and contain spherical bubbles (Fig. 5a), with calculated V_b/V_{MI} ratios (bubble volume/MI volume) between 0·03 and 0·12 (Table 4). It cannot be excluded that these bubbles contain a substantial fraction of volatiles (especially CO_2) initially dissolved in the entrapped melt (e.g. Frezzotti, 2001; Moore *et al.*, 2015; Wallace *et al.*, 2015; Robidoux *et al.*, 2017). Therefore, analysis of the glass gives only minimum volatile concentrations in the parent melt. Some MIs exhibit very small opaque oxides (Cr–Mg spinels), as previously found in other inclusions from the same deposit (Gennaro *et al.*, 2019).

The chemical compositions of the investigated FS MIs, together with their volatile abundances, are reported in Table 4. The major element compositions have been corrected for post-entrapment crystallization (PEC %, Table 4) following Gennaro *et al.* (2019) and references therein. Volatile contents are not corrected for PEC, as this would increase measured volatile contents only by relatively low amounts that are comparable with analytical uncertainties (Gennaro *et al.*, 2019).

As already shown by previous studies (Kamenetsky *et al.*, 2007; Corsaro & Métrich, 2016; Gennaro *et al.*, 2019), MIs of the FS eruption present high CaO (11·9–16·3 wt%) and MgO (8·6–10·9 wt%) contents, high CaO/Al_2O_3 ratio (0·9–1·5), low alkali contents (2·6–4·1 wt%), and high volatile abundances (H_2O = 1·9–5·9 wt%, CO_2 = 687–2786 ppm, S = 235–3445 ppm, Cl = 1165–3123 ppm). These chemical features identify FS MIs as the most primitive Etnean melts determined so far.

These FS MIs are used for the Fe speciation investigation (see following section), together with other Etnean MIs and one embayment, already characterized by Gennaro *et al.* (2019) for their major element compositions and volatile contents (Table 4). These samples belong to Mt Spagnolo (Fo_{82}), 2002–2003 ($Fo_{72–74}$), 2006 ($Fo_{70–81}$), 2008–2009 ($Fo_{69–75}$) and 2013 ($Fo_{70–72}$) eruptions (Fig. 5c and d), and have volatile contents generally lower than FS MIs (Table 4). Nevertheless, MIs from 2006 and Mt Spagnolo eruptions have been shown to have the highest S content (~4000 ppm, Moretti *et al.*, 2018; Gennaro *et al.*, 2019) among all the investigated MIs. Unfortunately, the MIs with the highest volatile contents were not available or had strongly olivine-contaminated XANES signals.

$Fe^{3+}/\Sigma Fe$ ratios of the MIs

$Fe^{3+}/\Sigma Fe$ ratios measured by XANES in the double-polished MIs range from 0·168 to 0·358 (Table 5, Figs 6 and 7): FS MIs exhibit the highest $Fe^{3+}/\Sigma Fe$ ratios (0·274–0·358), whereas 2008–2013 MIs generally have the lowest values (0·168–0·225).

$Fe^{3+}/\Sigma Fe$ ratios do not show any clear relation with the estimated percentage of PEC (Fig. S3 in Supplementary Data Electronic Appendix 2), therefore an important effect of post-entrapment crystallization on the estimated $Fe^{3+}/\Sigma Fe$ can be excluded. Nevertheless, following the approach of Hartley *et al.* (2017), which estimates the effect of olivine crystallization in the MI wall on the Fe^{3+} of the entrapped melt, we have corrected the $Fe^{3+}/\Sigma Fe$ for PEC (Table 4). For the MI with the highest PEC (14 %), the $Fe^{3+}/\Sigma Fe$ ratio would be lowered by an absolute value of 0·06 with respect to the estimated XANES value. Other mechanisms, such as H^+ diffusion through olivine or volatile loss (e.g. Gaetani & Watson, 2000; Frezzotti, 2001; Danyushevsky & Plechov, 2011; Bucholz *et al.*, 2013), could modify the $Fe^{3+}/\Sigma Fe$ ratio of the melt after its entrapment. The H^+ diffusion through the olivine crystal could result in the oxidation of the system and the formation of magnetite dust (e.g. Frezzotti, 2001; Danyushevsky *et al.*, 2002), which is not found in the investigated MIs.

Table 4: Chemical composition and volatile (H_2O, CO_2, S, Cl) contents of Etnean melt inclusions, one embayment and one matrix glass

Sample	Fo (mol%)	SiO_2	TiO_2	Al_2O_3	FeO_{tot}	MnO	MgO	CaO	Na_2O	K_2O	Cr_2O_3	P_2O_5	Total	PEC %	H_2O	CO_2 (ppm)	S (ppm)	Cl (ppm)	Mg#	V_b/V_{MI}	Size (μm) MI max.	P (MPa)	Depth (km)
FS-XS_8* [4]	90	48·5 (0·4)	1·1 (0·2)	11·4 (0·2)	9·5 (0·3)	0·2 (0·1)	10·9 (0·2)	14·8 (0·1)	2·0 (0·1)	1·0 (0·1)	b.d.l.	0·6 (0·2)	92	1·5	5·77 (±0·04) [2]	2652 (±171) [2]	2330 (±110)	1820 (±140)	74·8	0·04	128	266	10·3
FS-XS_15* [4]	90	50·6 (0·3)	1·2 (0·2)	11·7 (0·2)	8·3 (0·6)	0·1 (0·0)	9·9 (0·3)	13·0 (0·4)	2·3 (0·1)	1·8 (0·1)	0·1 (0·0)	0·9 (0·1)	95	3·3	1·93 (±0·05) [3]	900 (±17) [3]	235 (±77)	1570 (±80)	74·5	0·03	225	129	5·0
FS-XS_20* [4]	90	49·3 (1·0)	1·0 (0·1)	10·7 (0·5)	8·8 (0·3)	0·1 (0·0)	10·7 (0·2)	16·0 (0·3)	2·0 (0·2)	0·8 (0·0)	0·1 (0·0)	0·4 (0·2)	90	7·4	2·81 (±0·07) [3]	1526	2980 (±178)	2688 (±74)	77·2	0·04	62·5	161	6·2
FS-XS_22a* [4]	90	49·1 (0·3)	1·2 (0·1)	12·0 (0·4)	8·5 (0·3)	0·1 (0·1)	9·1 (0·4)	15·8 (0·2)	2·2 (0·1)	1·3 (0·2)	0·1 (0·0)	0·5 (0·0)	91	11·1	4·81 (±0·09) [2]	2786 (±289) [3]	3445 (±168)	2488 (±158)	73·1	0·05	96	272	10·5
FS-XS_22b* [4]	90	49·5 (0·6)	1·2 (0·1)	11·3 (0·9)	8·7 (0·7)	0·1 (0·0)	9·4 (1·0)	16·3 (0·3)	2·0 (0·2)	1·0 (0·2)	0·1 (0·0)	0·5 (0·2)	92	14·0	2·33 (±0·31) [2]	2033 (±131) [3]	2613 (±103)	1968 (±62)	74·2	0·04	48·5	203	7·8
FS-XS_26b* [3]	90	49·9 (0·5)	1·1 (0·0)	13·2 (0·2)	9·4 (0·4)	0·2 (0·1)	10·6 (0·0)	11·9 (0·2)	2·3 (0·1)	1·3 (0·1)	n.d.	0·2 (0·1)	95	8·3	2·86 (±0·05) [3]	b.d.l.	b.d.l.	b.d.l.	74·1	0·12	195	62†	2·4
FS-XS_28a* [3]	91	49·7 (0·2)	1·0 (0·1)	10·8 (0·1)	8·8 (0·4)	0·2 (0·1)	10·9 (0·3)	15·4 (0·1)	1·8 (0·1)	0·9 (0·0)	0·1 (0·0)	0·4 (0·1)	92	0·8	2·48 (±0·11) [2]	2079 (±17) [2]	2690 (±96)	1963 (±97)	77·4	0·05	64	221	8·5
FS-XS_28b* [3]	91	49·4 (0·2)	1·0 (0·2)	10·9 (0·3)	8·8 (0·2)	0·1 (0·1)	10·9 (0·2)	15·8 (0·1)	1·8 (0·0)	0·8 (0·2)	0·1 (0·0)	0·4 (0·1)	92	1·6	2·92 (±0·05) [2]	1892	2490 (±151)	3123 (±121)	76·9	0·07	95	201	7·7
FS-XS_30* [3]	90	50·2 (0·2)	0·9 (0·2)	11·7 (0·5)	8·7 (0·3)	0·2 (0·0)	10·5 (0·6)	14·4 (0·2)	2·0 (0·1)	1·0 (0·1)	0·1 (0·0)	0·3 (0·1)	92	9·8	2·51 (±0·06) (2)	1106	2308 (±166)	1653 (±90)	76·0	0·06	84	157	6·1
FS-XS_35* [3]	90	51·3 (0·2)	1·0 (0·1)	12·0 (0·1)	7·9 (0·3)	0·1 (0·1)	8·6 (0·1)	15·8 (0·0)	2·1 (0·0)	1·0 (0·1)	b.d.l.	0·2 (0·1)	92	10·3	3·99 (±0·02) (2)	1632 (±61) (2)	2460 (±145)	1507 (±196)	74·3	0·07	75·5	231	8·9
FS-XS_41* [4]	90	49·7 (0·4)	0·9 (0·1)	11·3 (0·2)	9·1 (0·5)	0·2 (0·1)	10·1 (0·5)	15·2 (0·5)	1·9 (0·0)	1·3 (0·0)	b.d.l.	0·3 (0·1)	94	1·6	4·31 (±0·02) [2]	687 (±207) [3]	1798 (±296)	1165 (±147)	73·4	0·08	160	139	5·4
FS_00‡ [6]	90	51·7 (0·3)	0·9 (0·2)	11·1 (0·1)	8·9 (0·4)	0·1 (0·1)	9·8 (0·1)	14·3 (0·2)	2·1 (0·1)	0·9 (0·1)	0·1	b.d.l.	95	0·1	3·70 (±0·05) [2]	882 (±93) (2)	1100 (±179)	1633 (±151)	73·0	0·20	180	167	6·4
Spa_3n‡ [3]	82	48·9 (0·0)	1·6 (0·2)	16·9 (0·0)	9·5 (0·8)	0·2 (0·1)	5·7 (0·2)	9·9 (0·1)	4·5 (0·0)	2·0 (0·1)	b.d.l.	0·6 (0·1)	97	8·4	0·16 (±0·07) [2]	b.d.l.	1515 (±49)	2280 (±156)	62·4	0·16	90	6†	0·2
2002_26‡ [2]	73	51·7 (0·9)	2·1	16·6 (0·4)	9·5 (0·3)	0·1 (0·1)	3·2 (0·1)	6·8 (0·2)	5·2 (0·2)	3·9 (0·2)	b.d.l.	0·9 (0·1)	95	0·0	0·36 (±0·02) [3]	b.d.l.	225 (±78)	1560 (±184)	43·2	0·04	130	7†	0·3
2002_30‡ (4)	74	52·2 (2·1)	1·4 (0·2)	17·6 (0·5)	9·3 (0·6)	0·2 (0·1)	3·9 (0·1)	6·5 (0·1)	5·1 (0·1)	2·9 (0·1)	n.d.	1·0 (0·1)	96	0·0	1·06	b.d.l.	343	2018	49·1	0·00	44	27†	1·0
2002_32 matrix gl† [2]	73	49·8 (0·2)	2·0 (0·3)	16·1 (0·2)	10·5 (0·4)	0·3 (0·0)	3·8 (0·0)	8·4 (0·1)	4·9 (0·6)	3·3 (0·1)	n.d.	1·0 (0·1)	95	—	b.d.l.	b.d.l.	b.d.l.	1330 (±93)	44·9	—	—	—	—
2006_4‡ [2]	71	51·4 (0·0)	1·7 (0·1)	16·3 (0·1)	10·6 (0·0)	0·1 (0·1)	3·8 (0·0)	8·1 (0·1)	4·8 (0·0)	2·4 (0·0)	n.d.	0·9	96	0·0	0·92 (±0·02) [2]	470	380 (±28)	2390 (±226)	46·2	—	100	64	2·5
2006_7em-b‡ [2]	8	49·5 (0·0)	1·9 (0·1)	16·8 (0·3)	11·0 (0·4)	0·3 (0·0)	3·5 (0·1)	8·8 (0·0)	4·5 (0·2)	3·4 (0·0)	n.d.	0·2	97	0·0	0·36	b.d.l.	525 (±262)	2240(±240)	42·1	—	—	7†	0·3
2008_1‡ [9]	75	50·1 (0·3)	2·1 (0·1)	17·3 (0·2)	9·1 (0·4)	0·2 (0·1)	3·5 (0·1)	8·9 (0·2)	4·8 (0·1)	2·9 (0·2)	n.d.	1·0	98	0·9	0·13	430 (±64) [2]	284 (±6)	b.d.l.	45·5	—	140	43	1·7
2008_6A‡ [3]	70	54·9 (0·8)	0·9 (0·1)	18·0 (0·1)	7·2 (0·6)	0·2 (0·1)	2·2 (0·0)	7·7 (0·2)	4·4 (0·1)	3·4 (0·2)	n.d.	1·1	100	3·7	b.d.l.	b.d.l.	153 (±216)	1869 (±76)	40·7	0·01	40	n.d.	n.d.
2013_30‡ [2]	72	50·8 (0·3)	1·5 (0·0)	19·2 (0·0)	7·1 (0·0)	0·2 (0·1)	2·4 (0·1)	8·6 (0·3)	6·1 (0·3)	3·2 (0·1)	n.d.	0·9 (0·1)	96	0·0	0·14	b.d.l.	310	2675	41·8	0·11	70	4†	0·2
2013_33‡	70	52·7	0·9	21·2	4·9	0·1	1·5	3·1	8·4	5·8	n.d.	1·4	99	0·5	0·08	b.d.l.	137	1867	40·8	0·04	116	2†	0·1
2013_34‡ [2]	71	54·0 (0·2)	1·6 (0·1)	20·2 (0·2)	6·3 (0·0)	0·2 (0·1)	2·0 (0·0)	5·2 (0·1)	6·4 (0·1)	3·9	n.d.	0·2	96	1·9	0·13	b.d.l.	270 (±51)	3350 (±114)	41·9	—	48	4†	0·2

All oxides (expressed in wt%) and Cl contents (ppm) are from EMP analysis. H_2O (wt%) and CO_2 (ppm) evaluated in this study are from FTIR, whereas S and Cl concentrations are from EMP. Major elements are normalized to 100 % on volatile-free basis, and corrected for PEC [PEC % is the estimated amount (wt%) of post-entrapment crystallization]. Volatiles are not corrected for PEC. Fo (mol%) is the forsterite content of the host olivine. Mg# is calculated as molar MgO/(FeO + MgO) ratio, with FeO as Fe^{2+}. V_b/V_{MI} is the ratio of the bubble (inside the MI) volume to the MI volume. The number in square brackets in the first column indicates the number of EMP analyses; the number in square brackets in the columns for H_2O and CO_2 indicates the number of FTIR or SIMS analyses. Standard deviations (1σ) are given for each oxide in parentheses. Total is the total sum of major oxides as obtained by EMP before the normalization to 100 wt%. b.d.l., below detection limit; n.d., not determined. Standard deviations are given precisely as the digits shown and values of 0·0 represent values <0·05 rounded down.

*Data from this study.

†Pressure and relative depth (below crater level) are calculated using 50 ppm of CO_2, considering the estimated CO_2 detection limit of the FTIR method (e.g. Cecchetti *et al.*, 2002; Von Aulock *et al.*, 2014).

‡Data from Gennaro *et al.* (2019).

Table 5: XANES $Fe^{3+}/\Sigma Fe$ ratios and estimated oxygen fugacity (fO_2) determined for Etnean MIs, one embayment of the 2006 eruption, and one matrix glass in the 2002 sample

Sample name	Fo (mol%)	S (ppm)	±	$Fe^{3+}/\sum Fe$	±	log fO_2	ΔNNO	Note
FS-XS_8	90	2330	110	0·306	0·013	–6·6	1·1	2018
FS-XS_15	90	235	77	0·274	0·013	–7·0	0·7	2018
FS-XS_20	90	2980	178	0·352	0·013	–6·3	1·4	2018
FS-XS_22a	90	3445	165	0·327	0·013	–6·5	1·2	2018
FS-XS_22b	90	2613	103	0·329	0·013	–6·6	1·2	2018
FS-XS_26b	90	b.d.l.	—	0·301	0·013	–6·6	1·1	2018
FS-XS_28a	91	2690	96	0·358	0·013	–6·2	1·6	2018
FS-XS_28b	91	2490	151	0·336	0·013	–6·4	1·3	2018
FS-XS_30	90	2308	166	0·321	0·013	–6·5	1·2	2018
FS-XS_35	90	2460	145	0·333	0·013	–6·5	1·2	2018
FS-XS_41	90	1798	296	0·287	0·013	–6·9	0·8	2018
FS_00*	90	1100	179	0·277	0·013	–7·0	0·7	2018
Spa_3n*	82	1515	49	0·328	0·004	–6·8	1·4	2015
2002_26*	73	225	78	0·200	0·004	–8·7	–0·3	2015
2002_30*	74	343	74	0·229	0·013	–8·1	–0·4	2018
2002_32 matrix gl*	73	b.d.l.	—	0·206	0·004	–9·3	–0·6	2015
2006_4*	70	380	28	0·248	0·004	–7·9	0·4	2015
2006_7emb*	81	525	262	0·212	0·004	–8·8	–0·2	2015
2008_1*	75·	284	6	0·168	0·004	–9·5	–0·8	2015
2008_6A*	69	153	216	0·209	0·004	–8·7	–0·2	2015
2013_30*	72	310	—	0·177	0·004	–9·5	–0·9	2015
2013_33*	70	137	51	0·225	0·013	–8·9	–0·4	2018
2013_34*	71	270	—	0·214	0·004	–8·8	–0·2	2015

$Fe^{3+}/\Sigma Fe$ ratios are obtained from XANES spectra acquired during 2015 and 2018 sessions (see main text and Supplementary Data Electronic Appendix 1 for details). The log fO_2 values are calculated from $Fe^{3+}/\Sigma Fe$ ratios using the empirical equation of Kress & Carmichael (1991) [equation (2)] in a temperature range of 1050–1200 °C and a pressure estimated from H_2O and CO_2 contents (see text for calculation details and Table 5). The error associated with the calculated NNO value is between 0·1 and 0·2, depending on the error associated with the $Fe^{3+}/\Sigma Fe$ ratio (±0·004 to ±0·013). emb, embayment; gl, glass; b.d.l., below detection limit.
*Fo (forsterite content of the host olivine) and S (ppm) data are from Gennaro *et al.* (2019).

Among the investigated melt inclusions, high values of PEC are estimated for both Mt Spagnolo and FS (Table 4). We used an independent oxybarometer (Ballhaus *et al.*, 1990, 1991) to estimate the fO_2 of Mt Spagnolo and FS magmas from mineral equilibria (see next section), and show that post-entrapment modifications of the $Fe^{3+}/\Sigma Fe$ ratio are likely to be negligible.

The $Fe^{3+}/\Sigma Fe$ ratios generally decrease with decreasing CaO/Al_2O_3 ratios and MgO content (Fig. 6a and b), and with increasing K_2O, Na_2O and SiO_2 contents (Fig. 6c–e). Less clear is the variation with the FeO_{tot} (Fig. 6f), suggesting an influence of the crystallization of Fe-bearing minerals on the $Fe^{3+}/\Sigma Fe$ ratio. No clear correlation is visible between $Fe^{3+}/\Sigma Fe$ ratios and abundances of H_2O, S, Cl and CO_2 (Fig. 7), nor with the estimated storage pressure (Fig. 8). Only FS MIs generally show higher H_2O, CO_2 and S contents and $Fe^{3+}/\Sigma Fe$ ratios than more evolved MIs (Fig. 7). These observations suggest that the variation of the melt $Fe^{3+}/\Sigma Fe$ ratio is negligibly affected by decompression and degassing.

Redox conditions of Etnean magmas

$Fe^{3+}/\Sigma Fe$ ratios determined by XANES for the MIs of FS, Mt Spagnolo and 2002–2013 eruptions (Table 5) are used for estimating the redox conditions of the magmas feeding these eruptions, through equation (2).

Oxygen fugacity estimations for Etnean MIs are reported in Table 5, expressed as deviation from the NNO buffer (ΔNNO). For these calculations, we used the pressure values estimated from the H_2O–CO_2 contents (Table 4), and temperatures of 1200 °C for FS (Mollo *et al.*, 2015), 1170–1180 °C for Mt Spagnolo (Kamenetsky & Clocchiatti, 1996) and 1130–1150 °C for the other eruptions (e.g. Kahl *et al.*, 2011, 2015; Mollo *et al.*, 2015).

FS MIs show the highest values (NNO + 0·7 to NNO + 1·6), together with the only MI from Mt Spagnolo eruption (NNO + 1·4), whereas the lowest values (NNO – 0·9 to NNO – 0·2) are observed for MIs from 2008 and 2013 eruptions (Fig. 9a).

Previous studies estimated redox conditions between NNO and NNO + 1·8 (Fig. 9b), based on phase–silicate melt and phase–phase equilibria (e.g. Trigila *et al.*, 1990; Armienti *et al.*, 1994; Kamenetsky & Clocchiatti, 1996; Métrich & Rutherford, 1998; Kahl *et al.*, 2011), or between NNO and NNO + 1 based on S speciation (Métrich & Clocchiatti, 1996; Métrich *et al.*, 2009; Morizet *et al.*, 2017).

In addition to the $Fe^{3+}/\Sigma Fe$ ratio, we applied other methods to estimate the redox conditions for the same group of samples. The oxybarometer method of Arató & Audétat (2017) was used on magnetite-bearing samples to estimate oxygen fugacity from the partitioning of Fe and Ti between magnetite and silicate melt (FeTiMM; Table S2 in Supplementary Data Electronic Appendix 2). The calculations suggest ΔNNO from –0·9 to +0·5 for the 2002 MIs, from –0·26 to +0·66 for the 2006 MIs, from –1·47 to +0·85 for the 2008 MIs, and

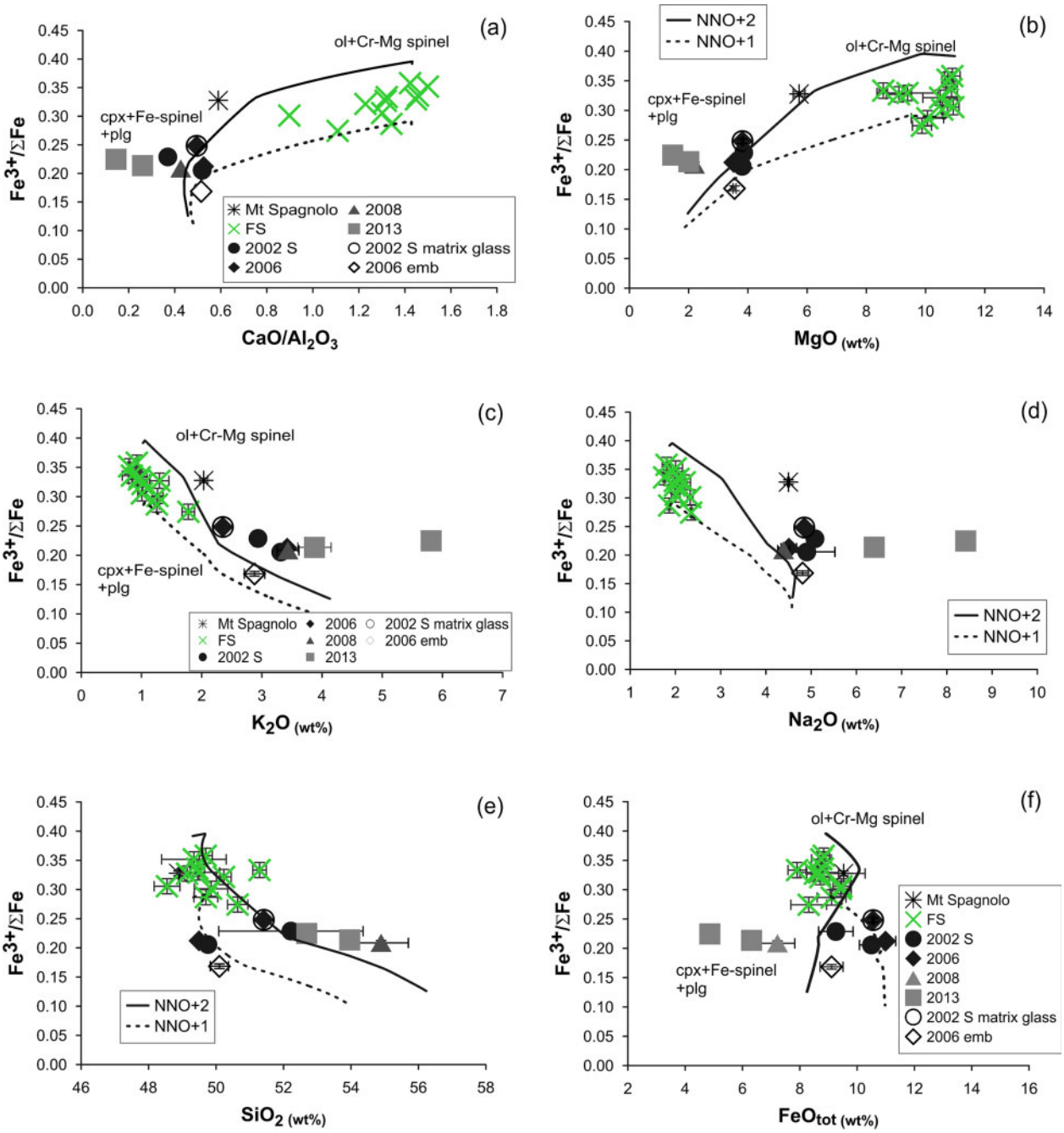

Fig. 6. $Fe^{3+}/\Sigma Fe$ ratios determined by XANES spectroscopy for Etnean MIs, the embayment (emb) and the matrix glass, as a function of (a) CaO/Al_2O_3 ratios, (b) MgO, (c) K_2O, (d) Na_2O, (e) SiO_2, and (f) FeO_{tot} contents in glass. The error bars indicate the standard deviation (1σ). The two black curves indicate the liquid lines of descend calculated by MELTS code (Ghiorso & Sack, 1995; Smith & Asimow, 2005) during fractional crystallization of ol + Mg–Cr-spinel → Fe-spinel + cpx + plg (plg only at the advanced step of fractional crystallization). (See main text for details on this modelling.) The two curves illustrate the simulations performed using a $dP/dT = 3\,MPa\,^{\circ}C^{-1}$, and an initial fO_2 of NNO + 1 (dashed line) or NNO + 2 (continuous line).

from –1·09 to +0·70 for the 2013 MIs (Fig. 9c, Table S2 in Supplementary Data Electronic Appendix 2). For four of the magnetite–MI pairs, the XANES $Fe^{3+}/\Sigma Fe$ ratios in the corresponding MI are known and the fO_2 values estimated with the two methods are shown in Fig. 9c (and presented in Table S2 in Supplementary Data Electronic Appendix 2).

The oxygen thermo-oxybarometer of Ballhaus *et al.* (1990) modified by Ballhaus *et al.* (1991), based on the olivine–spinel equilibrium, was applied only to the Cr-spinel–olivine pairs from Mt Spagnolo and FS rocks (Table S2 in Supplementary Data Electronic Appendix 2). The calculations yields fO_2 of NNO + 1·5 ± 0·1 for both Mt Spagnolo and FS (Fig. 9c and Table S2), which

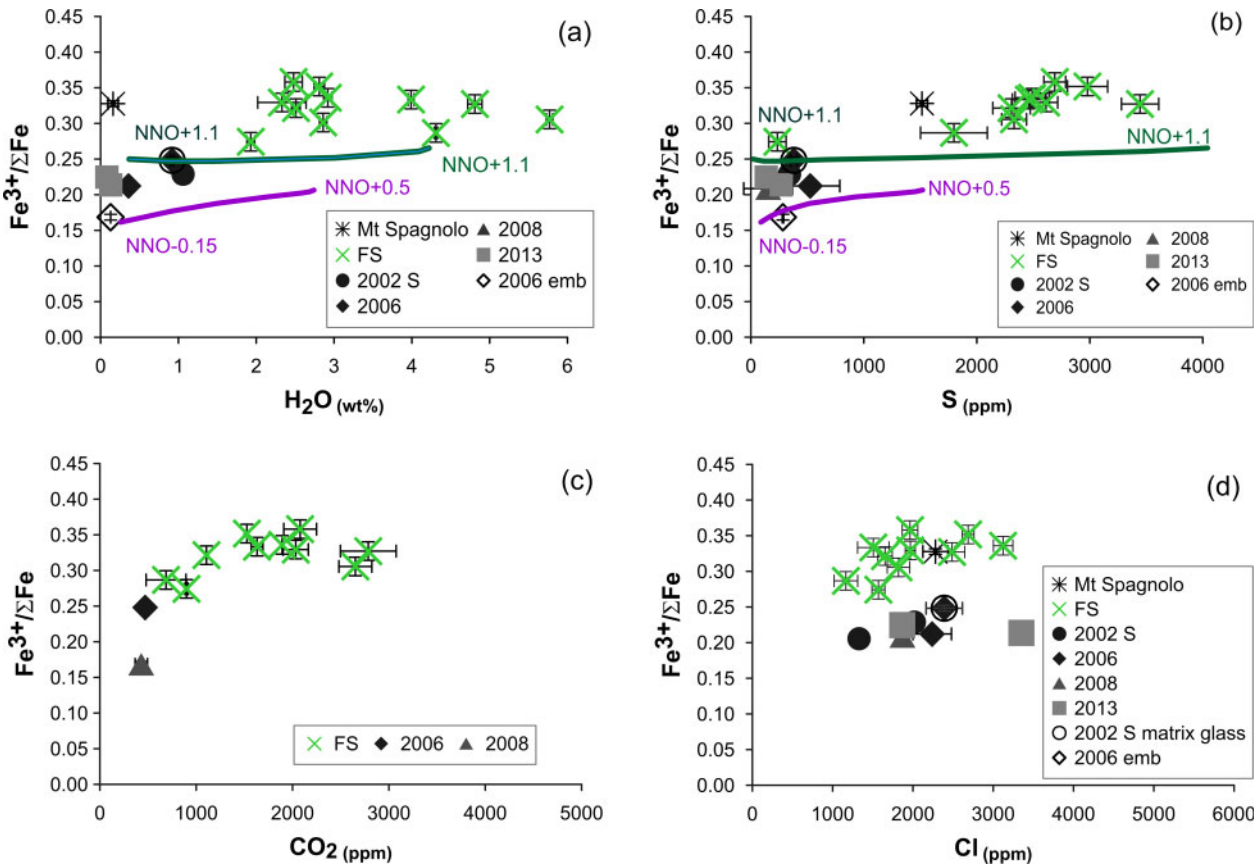

Fig. 7. $Fe^{3+}/\Sigma Fe$ ratios determined by XANES spectroscopy for MIs, one embayment in 2006–2007 olivine and one matrix glass for 2002 sample versus their relative (a) H_2O, (b) S, (c) CO_2 and (d) Cl contents. Degassing curves for H_2O (a) and S (b) are modelled using the approach of Gaillard & Scaillet (2009) and Gaillard *et al.* (2011). The initial conditions of the simulations are given in the text and reported in Table S3 (in Supplementary Data Electronic Appendix 2).

are in good agreement with those based on the XANES $Fe^{3+}/\Sigma Fe$ ratios. This indicates that post-entrapment modifications have a negligible effect on the $Fe^{3+}/\Sigma Fe$ ratio of the MIs, even when PEC exceeds 10 %. More generally, our fO_2 estimations are close to those from previous studies (Fig. 9b), some of which applied to the products of the same eruptions (~NNO to NNO + 2; e.g. Trigila *et al.*, 1990; Armienti *et al.*, 1994; Kamenetsky & Clocchiatti, 1996; Métrich & Clocchiatti, 1996; Métrich & Rutherford, 1998; Métrich *et al.*, 2009; Kahl *et al.*, 2011; Morizet *et al.*, 2017). What is evident in Fig. 9 is that the determined redox conditions for Etnean product span a very wide range of fO_2; that is, from NNO − 1·5 to NNO + 1·8.

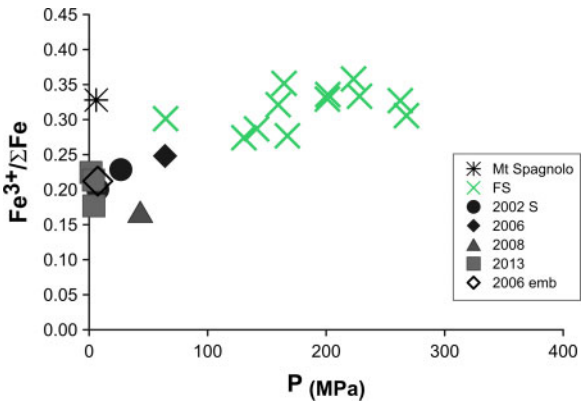

Fig. 8. $Fe^{3+}/\Sigma Fe$ ratios determined by XANES spectroscopy for Etnean MIs and the embayment (emb) of 2006–2007 olivine as a function of pressure (Table 4, this study; Gennaro *et al.*, 2019), estimated from H_2O and CO_2 concentrations using the Iacono Marziano *et al.* (2012) fluid–melt saturation model.

DISCUSSION

Differentiation and degassing processes in Etnean magmas

MgO-rich olivine crystals of the FS eruption entrap the most primitive MIs among those of Mt Etna (e.g. Kamenetsky & Clocchiatti, 1996; Métrich *et al.*, 2004; Spilliaert *et al.*, 2006*a*; Kamenetsky *et al.*, 2007; Collins *et al.*, 2009; Schiavi *et al.*, 2015; Corsaro & Métrich, 2016; Moretti *et al.*, 2018; Gennaro *et al.*, 2019). These MIs are very rich in volatiles, and their minimum entrapment pressures, retrieved from their H_2O and CO_2 contents using the solubility model of Iacono Marziano *et al.* (2012), range from 62 to 272 MPa (Table 4). Using a rock density of 2·65 g cm^{-3} as an average for the different lithologies of the crustal basement [from 2·57 to 2·70 g cm^{-3} in the first 22 km of the crust, as reported by

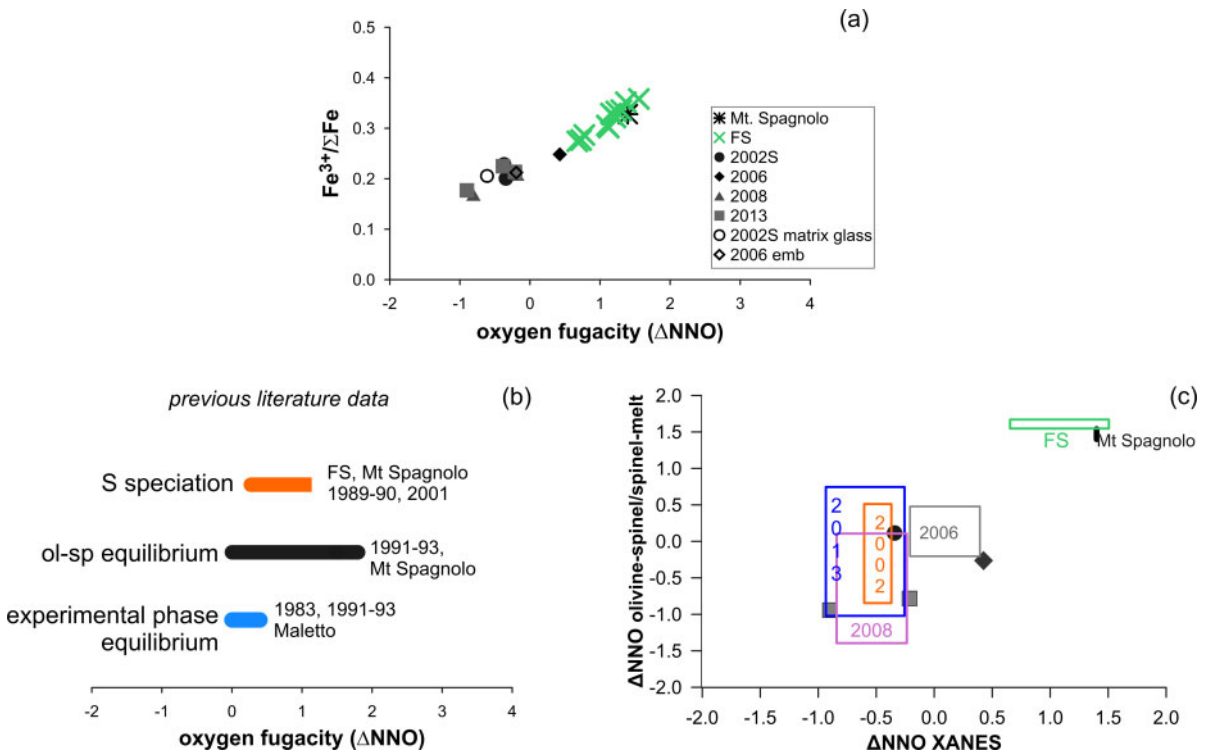

Fig. 9. (a) Estimates of oxygen fugacity (expressed as ΔNNO, as defined in the caption of Fig. 2 and in the main text) for the studied eruptions of Mt Etna from $Fe^{3+}/\sum Fe$ ratios obtained by XANES. (b) Estimates of oxygen fugacity for Mt Etna from previous studies: S speciation (Métrich & Clocchiatti, 1996; Métrich *et al.*, 2009; Morizet *et al.*, 2017), experimental phase equilibria (Trigila *et al.*, 1990; Armienti *et al.*, 1994; Métrich & Rutherford, 1998), olivine–spinel equilibria (Kamenetsky & Clocchiatti, 1996; Kahl *et al.*, 2011). (c) Comparison of fO_2 estimates from XANES data with those from the oxybarometer methods of Ballhaus *et al.* (1990, 1991) and Arató & Audétat (2017).

Corsaro & Pompilio (2004)], these pressures correspond to depths varying from 2·4 to 10·5 km below crater level ('bcl'), which are inside the range of previous estimations (4–19 km bcl, e.g. Kamenetsky *et al.*, 2007; Gennaro *et al.*, 2019). Gennaro *et al.* (2019) proposed that magmas feeding Etnean eruptions in the last 15 kyr could have been produced by variable amounts of differentiation of a parental melt with the composition of the most primitive FS MIs ('FS-type magma'), on the basis of differentiation trends observed in MIs and MELTS simulations. Without excluding the occurrence of additional processes (such as mixing events, sulphate assimilation, alkali enrichments, mantle metasomatism or different melting degrees of the mantle source) to thoroughly explain the chemical variability of Etnean magmas, Gennaro *et al.* showed that MELTS simulations of fractional crystallization of FS-type magma capture most of the first-order features of the Etnean magmas erupted in the last 15 kyr (Gennaro *et al.*, 2019). We therefore consider FS most primitive MIs as possible parental melt for the following discussion and modelling.

Variability in Etnean magmatic redox conditions

$Fe^{3+}/\sum Fe$ ratios obtained by XANES spectroscopy for Etnean MIs yield a large range of fO_2 values (NNO − 1·5 to NNO + 1·6 of fO_2) that is corroborated by two independent oxybarometers (magnetite–silicate melt equilibrium, and olivine–spinel equilibrium, see 'Redox conditions of Etnean magmas' section). These data significantly enlarge the range of previous estimations (∼NNO to NNO + 2; e.g. Trigila *et al.*, 1990; Armienti *et al.*, 1994; Kamenetsky & Clocchiatti, 1996; Métrich & Clocchiatti, 1996; Métrich & Rutherford, 1998; Métrich *et al.*, 2009; Kahl *et al.*, 2011; Morizet *et al.*, 2017) as shown in Figure 9.

In the following, we will explore two main processes that could explain these variations observed in Etnean magmas: volatile degassing and melt evolution.

Effects of volatile degassing on redox conditions

Several recent studies have discussed the effect of volatile degassing on the variation of the magmatic redox state (e.g. Burgisser & Scaillet, 2007; Gaillard *et al.*, 2011; Moussallam *et al.*, 2014, 2016; Waters & Lange, 2016).

The effect of the degassing of H_2O and CO_2 on the magmatic redox state is controversial, as it is proposed to either oxidize the magma (e.g. Mathez, 1984; Burgisser & Scaillet, 2007; Humphreys *et al.*, 2015) or reduce it (e.g. Wilke *et al.*, 2002), or have no effect on it (Kelley & Cottrell, 2012; Waters & Lange, 2016), depending on melt and fluid phases composition. Indeed, for a silicic melt composition, degassing of a H_2O–CO_2 fluid

phase is expected to oxidize the melt (e.g. Burgisser & Scaillet, 2007; Humphreys *et al.*, 2015).

In the present case of the Etnean basaltic MIs, no clear correlation is observed between $Fe^{3+}/\Sigma Fe$ ratios and H_2O and CO_2 contents (Fig. 7a–c), and the drop of $Fe^{3+}/\Sigma Fe$ with entrapment pressure from FS toward 2008–2013 MIs (Fig. 8) suggests a reduction of the melt upon decompression and degassing. This, however, does not necessarily mean that H_2O and CO_2 degassing is the cause of the reduction.

Sulphur is known to have an important influence on magmatic redox conditions, owing to its varying oxidation states in the silicate melt and in the fluid phase (e.g. Burgisser & Scaillet, 2007; Gaillard & Scaillet, 2009; Métrich *et al.*, 2009; Gaillard *et al.*, 2011; Moussallam *et al.*, 2014, 2016, 2019), and with a difference of eight electrons between the most oxidized (S^{6+}) and the most reduced form (S^{2-}). The dominant S species measured in the volcanic gases is SO_2, whereas H_2S and S_2 are minor species (e.g. Oppenheimer, 2003). Although in recent experimental investigation at low temperature (650–950 °C) H_2S was shown to be the dominant S species at fO_2 between NNO and NNO + 0·7 and pressures between 50 and 200 MPa (Binder & Keppler, 2011), SO_2 degassing is increasingly favoured during magma ascent, as the homogenous equilibrium in gas phase shifts to the left with reducing pressure (Gaillard *et al.*, 2011):

$$SO_2 + 3H_2 = 2H_2O + H_2S. \quad (3)$$

According to Métrich *et al.* (2009), the degassing of SO_2 from an oxidized basaltic Fe-bearing melt, in which the dominant dissolved S species is sulphate [$(SO_4)^{2-}$], causes oxidation of dissolved iron and therefore an increase of Fe^{3+}/Fe^{2+}:

$$CaSO_{4(melt)} + 2Fe^{2+}O_{(melt)} = SO_{2(gas)} + Fe^{3+}{}_2O_{3(melt)} + CaO_{(melt)}. \quad (4)$$

Conversely, at more reduced redox conditions, the exsolution of S^{2-} from an Fe-bearing melt induces iron reduction and therefore a decrease of Fe^{3+}/Fe^{2+}:

$$Fe^{2+}S^{2-}{}_{(melt)} + 3Fe^{3+}{}_2O_{3(melt)} = SO_{2(gas)} + 7Fe^{2+}O_{(melt)}. \quad (5)$$

Moussallam *et al.* (2014, 2016) observed a strong reduction of the redox condition of the melt driven by sulphur degassing at Erebus and Kilauea volcanoes, starting from variable redox conditions (around NNO for Kilauea, and >NNO + 1 for Erebus melts).

To verify the effect of degassing on the iron speciation ($Fe^{3+}/\Sigma Fe$) of the Etnean magmas, we modelled the degassing of H_2O (the most abundant volatile in magma) and S (the only polyvalent volatile species) using the gas–melt equilibrium models of Gaillard & Scaillet (2009) and Gaillard *et al.* (2011). Two simulations were performed: one started from a fO_2 of NNO + 1·1 (at which S in the melt is preferentially in its oxidized form, SO_4^{2-}), an initial P of 400 MPa, and H_2O and S contents in the melt of 4 wt% and 4000 ppm, respectively; the second simulation started from a fO_2 of NNO + 0·5 (at which a more important portion of the S dissolved in the melt is in its reduced form S^{2-}), an initial P of 150 MPa, and H_2O and S contents in the melt of 3 wt% and 1500 ppm, respectively. The temperature (kept constant during the decompression) was 1200 °C and 1150 °C, respectively (details of the calculations are given in Table S3 in Supplementary Data Electronic Appendix 2). In both simulations, S degassing is indirectly caused by H_2O exsolution from the silicate melt, which in turn is triggered by decompression. The simulation performed in the most oxidizing redox conditions showed no variations in fO_2 induced by degassing, and generally reproduces the trend presented by FS MIs (green curves in Fig. 7a and b), even if it underestimates their $Fe^{3+}/\Sigma Fe$ ratios. This simulation cannot, however, describe the lower $Fe^{3+}/\Sigma Fe$ ratios shown by 2002–2013 MIs, the embayment and the matrix glass. In contrast, the simulation performed in the most reducing redox conditions (violet curves in Fig. 7a and b) predicts a slight decrease in the $Fe^{3+}/\Sigma Fe$ ratio induced by degassing, without, however, reproducing the whole trend shown by MIs (Fig. 7a and b).

These simulations suggest that the effect of S and H_2O degassing on the $Fe^{3+}/\Sigma Fe$ ratio of the Etnean magma is too small to be the only process controlling the important reduction (from NNO + 1·6 to NNO – 1·9) recorded by Etnean melt inclusions.

Effects of magma differentiation on redox conditions

The correlation between the $Fe^{3+}/\Sigma Fe$ ratio and several major oxides (Fig. 6) suggests that the variation of the magmatic redox conditions may be related to melt differentiation. For example, the $Fe^{3+}/\Sigma Fe$ ratio of the MIs decreases with decreasing MgO content and CaO/Al_2O_3 ratio, and with increasing SiO_2, K_2O and Na_2O contents (Fig. 6), as previously observed in other magmatic contexts (Kelley & Cottrell, 2012) and in experimental investigations (e.g. Borisov & McCammon, 2010; Borisov *et al.*, 2015).

We used the MELTS code (Ghiorso & Sack, 1995; Smith & Asimow, 2005) to simulate fractional crystallization in open-system conditions upon simultaneous cooling and decompression (at a fixed dP/dT), starting from the most primitive composition of FS MIs (10·5 wt% MgO, 5 wt% H_2O). In this way, we estimated the evolution of the $Fe^{3+}/\Sigma Fe$ ratio of the residual liquid during the fractional crystallization as calculated by MELTS, and compared the results with the $Fe^{3+}/\Sigma Fe$ ratio estimated by XANES for the Etnean MIs (FS, Mt Spagnolo and 2002–2013 eruptions).

The imposed initial T–P values were 1200 °C and 400 MPa, which, together with a dP/dT of 3 MPa °C^{-1}, are the conditions that best reproduce the major element variations of the studied MIs according to Gennaro *et al.* (2019). Oxygen fugacity was allowed to freely

evolve during crystallization (i.e. unconstrained). Two initial fO_2 values were used (NNO + 1 and NNO + 2), to bracket the fO_2 estimations for FS MIs (~NNO + 1·5, Table 5 and Table S2 in Supplementary Data Electronic Appendix 2), considering the high uncertainty probably associated with this estimation (analytical errors, PEC, volatile diffusion, bubbles).

Both simulations predict a decrease of the $Fe^{3+}/\Sigma Fe$ ratio during fractional crystallization (continuous and dashed black curves in Fig. 6), which is dictated by the crystallizing phases (in the simulations only the initial oxygen fugacity is fixed). These variations generally reproduce well the trends shown by MIs, with the exception of the most evolved ones.

The early crystallization of olivine and Mg–Cr-spinel (Cr# = 55–65) at high T and P (1170–1200 °C and 250–400 MPa), calculated by the MELTS code, preferentially transfers Fe^{2+} into the solid phases, inducing a slight increase in the $Fe^{3+}/\Sigma Fe$ ratio in the residual melt, and a slight decrease in total iron, while MgO decreases from 11 to ~9 wt% (Fig. 6b–f). At lower temperatures and pressures, and for the most oxidizing redox conditions simulation, the $Fe^{3+}/\Sigma Fe$ ratio begins to decrease in response to the extensive clinopyroxene crystallization (Fig. 6), which probably consumes more Fe^{3+} than Fe^{2+} (O'Neill *et al.*, 2018). This is accompanied by an increase in total FeO content (continuous black curve in Fig. 6f). A more important decrease in the $Fe^{3+}/\Sigma Fe$ ratio is observed when magnetite starts to crystallize: $Fe^{3+}/\Sigma Fe$ ratios calculated by MELTS simulations decrease to value of ~0·13, which is slightly lower than the lowest $Fe^{3+}/\Sigma Fe$ ratios measured in our MIs (Fig. 6). At higher initial fO_2 (NNO + 2), Fe-spinel crystallization occurs at 1150 °C and ~6 wt% MgO, which sensibly decreases the FeO_{tot} content of the melt. At lower initial fO_2 (NNO + 1), spinel crystallization only occurs at 1085 °C and ~4 wt% MgO, which does not prevent the FeO_{tot} content of the melt increasing up to 10–12 wt%, as observed in 2002, 2006 and 2008/2009 MIs (Fig. 6b–f). Because the MgO and Cr contents of the residual melt decreased, the spinel crystallizing at this stage has a titano-magnetite composition, in agreement with the observations in 2002–2013 eruptive products (e.g. Kahl *et al.*, 2015; Mollo *et al.*, 2015; Schiavi *et al.*, 2015; Gennaro *et al.*, 2019). In contrast, in FS and Mt Spagnolo olivines, Cr-spinel are detected (e.g. Kamenetsky & Clocchiatti, 1996; Kamenetsky *et al.*, 2007; Gennaro *et al.*, 2019).

MIs from 2013 showed FeO_{tot} contents lower than those predicted by the MELTS models (Fig. 6f), whereas the $Fe^{3+}/\Sigma Fe$ ratio maintains a constant value (~0·21 ± 0·03), which could be due to a more copious crystallization of magnetite (and plagioclase) at constant fO_2 than that predicted by MELTS (Gennaro *et al.*, 2019). This could also explain the lower CaO/Al_2O_3 ratio of these MIs than the values calculated by the liquid line of descent (Fig. 6a). Furthermore, Fig. 6 reveals a discrepancy between alkali contents measured in MIs and those predicted by MELTS (Fig. 6c and d). The alkali contents of 2013 MIs, and to a lower extent those of Mt Spagnolo and 2002–2008 MIs, are generally higher than those of the liquid line of descent of FS magma, as already noted by Gennaro *et al.* (2019). Alkali enrichment of the Etnean magmas is highly debated. Among the numerous hypotheses, Correale *et al.* (2014) proposed that the variability of primitive whole-rock compositions requires variable melting degrees of a single mantle source, followed by crystallization. The enrichment in K_2O has also been attributed to the upward migration of deep Cl-rich fluids carrying alkalis (Ferlito & Lanzafame, 2010), supported by the variable and high Cl concentrations measured in MIs (up to 4600 ppm; e.g. Collins *et al.*, 2009; Moretti *et al.*, 2018; Gennaro *et al.*, 2019). A recent study shows that lowering of water activity during the fractional crystallization of a basaltic melt yields a decrease in MgO and a significant increase in K_2O relative to SiO_2 contents in the residual liquids (e.g. Beermann *et al.*, 2017).

The good agreement between the estimated $Fe^{3+}/\Sigma Fe$ ratios in MIs and the $Fe^{3+}/\Sigma Fe$ ratio variations (Fig. 6) calculated by the MELTS code for the residual melt during the fractional crystallization of olivine + Mg–Cr-spinel and cpx + Fe-spinel (+ plg) suggests that the variation in redox conditions of the Etnean magmas can be significantly affected by melt differentiation via fractional crystallization.

The occurrence of these mineral phases (ol, cpx, plg and Fe–Ti oxides) is common in basalts and trachybasalts erupted by Mt Etna in recent decades; a variability in redox conditions (between NNO and NNO + 2) is likely to influence the percentage and the composition of these minerals (e.g. Kamenetsky & Clocchiatti, 1996; Viccaro *et al.*, 2010; Armienti *et al.*, 2013; Kahl *et al.*, 2015; Giacomoni *et al.*, 2016).

Sulphur behaviour during fractional crystallization of fluid-saturated magmas

Sulphur behaviour in fluid-saturated magmas during crystallization is strictly linked to the proportions of its dissolved species (sulphate and sulphide), as they exhibit different solubilities and are therefore exsolved at different rates: sulphate is more soluble, whereas sulphide is more volatile and could degas more efficiently (e.g. Carroll & Rutherford, 1985, 1987; Luhr, 1990; Jugo *et al.*, 2005). Oxygen fugacity controls sulphur speciation in both the silicate melt (S^{2-} versus S^{6+}) and the fluid phase (H_2S versus SO_2) and, therefore, affects S degassing behaviour.

To model the sulphur behaviour during decompression and crystallization and, therefore, during decrease of T, P and fO_2, we calculated the S content of the residual liquid from the results of MELTS crystallization simulations, taking into account the variation of the experimentally determined S distribution coefficient between fluid and melt ($DS^{fluid/melt}$; see 'S content in the fluid phase and fluid/melt partitioning' section).

Although associated with large uncertainties, the constructed empirical model provides a suitable approach to estimate $DS^{fluid/melt}$ value in basaltic magmas as a function of the three intensive variables (T, P and fO_2).

We used (1) the crystallization simulation performed in T–P–fO_2 range of 1200–1068 °C, 400–0·1 MPa, NNO + 2 to NNO – 1·8 using MELTS code and a fixed dP/dT ratio of 3 MPa °C^{-1}, which well reproduces the chemical trends shown by the MIs (Fig. 6), and (2) an additional MELTS simulation performed in the same T–P–fO_2 range with a dP/dT ratio of 20 MPa °C^{-1}, which better reproduces the highest decompression rate experienced by FS magma (Gennaro *et al.*, 2019). Each step of MELTS simulations returns the composition of the residual liquids after crystallization owing to the ΔP–ΔT change corresponding to the considered dP/dT ratio.

For each step, the sulphur content of the residual melt (S_{MELTS}) is then calculated using the following equation:

$$S_{MELTS} = (S^*_{MELTS} \cdot M_{syst})/(M_{melt} + M_{fluid} \cdot DS^{fluid/melt}) \quad (6)$$

in which M_{syst}, M_{melt} and M_{fluid} are respectively the masses of the total system, the residual melt and the fluid phase and S^*_{MELTS} is the S content of the previous step in the MELTS simulation. As initial S^*_{MELTS} we used the maximum S content in the FS MIs (S = 3445 ppm, Table 4). M_{syst} and M_{melt} are calculated by MELTS code, whereas the mass of the fluid phase (M_{fluid}) is calculated in each step of MELTS simulation (n, $n+1$, $n+2$, …), as follows:

$$M_{fluid(n+1)} = (M_{melt} \cdot H_2O_{MELTS\ (n)}/100)_n - (M_{melt} \cdot H_2O_{MELTS\ (n+1)}/100)_{(n+1)} \quad (7)$$

where H_2O_{MELTS} is the H_2O content in the residual melt, calculated by MELTS code, at each step of fractional crystallization.

The S content obtained using equations (6) and (7) is shown in Figs 10 and 11 as a function of the MgO and K_2O contents of the melt, both being markers of melt differentiation, and of fO_2 variation.

The simulation using a dP/dT of 20 MPa °C^{-1} (red curve in Figs 10a, b and 11) describes a rapid decompression with a low fractional crystallization, and is accompanied by a slight decrease of fO_2 (from NNO + 2 to NNO + 1·5) and a continuous decrease of S content in the melt. The important S degassing is favoured by the significant pressure decrease, accompanied by H_2O exsolution, as also predicted by S–H_2O degassing simulations (Fig. 7a and b). The amount of S degassing simulated following this dP/dT rate (red curves in Figs 10 and 11) is analogous to that observed in FS MIs, which is accompanied by a decrease in fO_2 from NNO + 1·6 to NNO + 0·7 (Table 5). Based on this evidence, FS eruption is probably unique in the eruptive history of Etna and was most probably produced by an unusually strong and rapid decompression of the magma, inducing explosive CO_2–H_2O and S degassing.

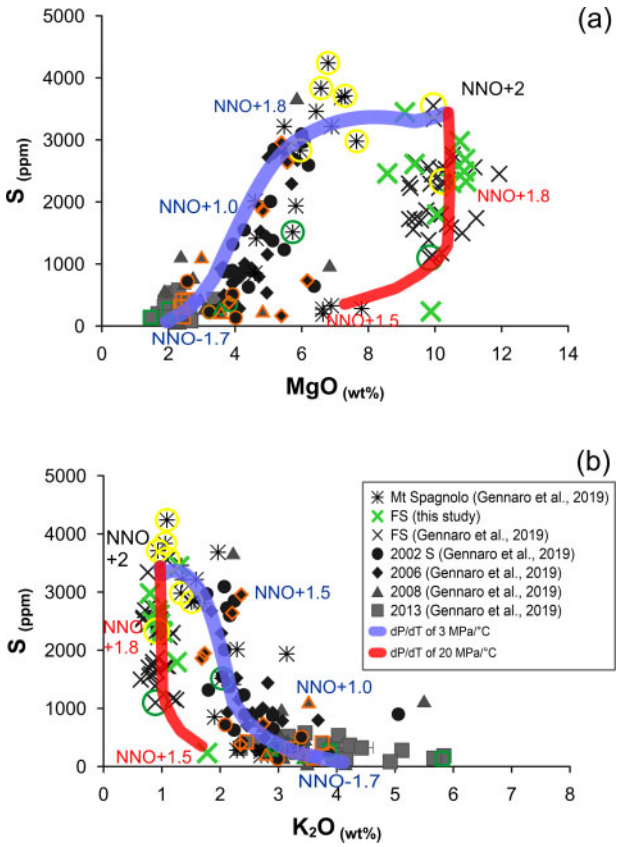

Fig. 10. S content versus (a) MgO and (b) K_2O contents of the MIs (data from this study and Gennaro *et al.*, 2019). The two coloured curves indicate S contents calculated coupling equations (6) and (7) to the MELTS simulations with dP/dT = 3 and 20 MPa °C^{-1} and initial fO_2 of NNO + 2 (during fractional crystallization of ol + Mg–Cr-spinel → Fe-spinel + cpx + plg). Outlined symbols indicate data from Gennaro *et al.* (2019) for which fO_2 values have been estimated using olivine–spinel equilibrium (in yellow), spinel–melt equilibrium (in orange), or XANES $Fe^{3+}/\Sigma Fe$ ratios (in green).

In contrast, the simulation performed using a dP/dT of 3 MPa °C^{-1} (blue curve in Figs 10a, b and 11) is characterized by major crystallization and subsequent fO_2 reduction (from NNO + 2 to NNO – 1·8). The S content of the melt slightly decreases during the early crystallization (of ol + Fe-oxide), when fO_2 is around NNO + 1·9 and the MgO content is higher than 9 wt% (Figs 6b, 10a and 11). At these conditions, neither decompression nor crystallization are effective for sulphate degassing.

When cpx starts to crystallize in major quantity, S initially slightly increases and then resumes decreasing. At a more advanced melt evolution (MgO content lower than 6 wt%, Fig. 10a), MELTS code calculates a decrease in fO_2 from NNO + 1·3 to NNO – 1·7, as a consequence of fractional crystallization of cpx + Fe–Ti-spinel (and at the final step, plg), which leads to an important S decrease in the silicate melt (Fig. 11). This trend is observed in 2002–2013 (and partially in Mt Spagnolo) MIs, which are characterized by a decrease in $Fe^{3+}/\sum Fe$

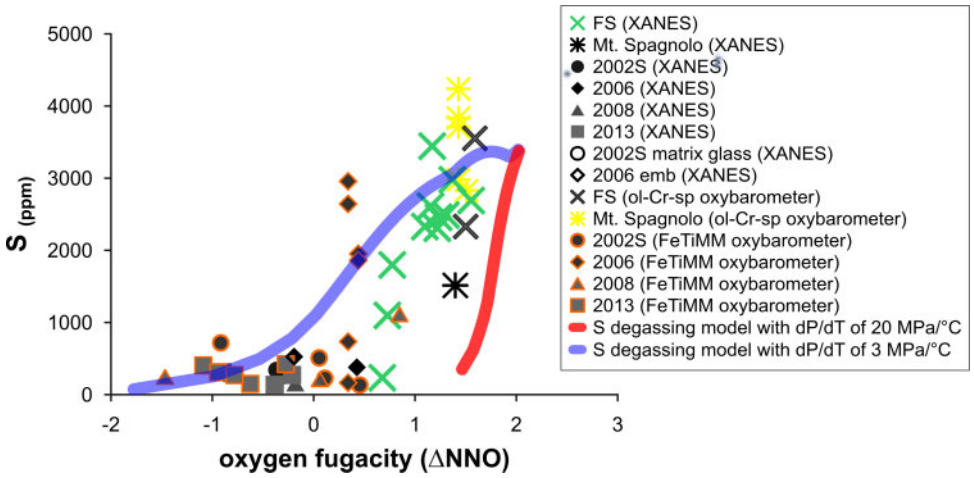

Fig. 11. S content of melt inclusions (together with embayment of 2006 and matrix glass of 2002 samples) versus oxygen fugacity (expressed as ΔNNO, as defined in the caption of Fig. 2 and in the main text), estimated from the XANES $Fe^{3+}/\Sigma Fe$ ratios and from oxybarometer methods of Ballhaus *et al.* (1990, 1991) and Arató & Audétat (2017). Also shown is the behaviour of S as a function of fO_2 variation, upon the liquid lines of descent modelled by MELTS code coupled to equations (6) and (7).

ratio from 0·25 to 0·17, corresponding to a decrease in fO_2 from NNO + 1 to NNO − 1·5 (Figs 6, 7 and 11, Table 5 and Table S2 in Supplementary Data Electronic Appendix 2). Therefore, whereas crystallization induces S enrichment in the melt, the conversion of sulphate to scarcely soluble sulphide causes extensive degassing and a drastic drop of the S content in the melt (down to <100 ppm at log fO_2 < NNO, Fig. 11).

The variability shown by the MIs of the same eruption could reflect the effects of other volatiles, such as CO_2 and Cl, on S degassing. These volatiles are not accounted for by the $DS^{fluid/melt}$ calibration model presented here, and could influence the $DS^{fluid/melt}$ (e.g. Beermann *et al.*, 2015; Fiege *et al.*, 2015).

In conclusion, as suggested by our and previous (e.g. Beermann *et al.*, 2011, 2015; Lesne *et al.*, 2011*a*; Fiege *et al.*, 2015) experimental results, oxygen fugacity probably exerts the major control on the S content of Etnean melts, and ensures efficient S degassing during magma ascent.

Most of the MIs presented in Figs 10 and 11 do not contain sulphide globules, which were observed only in a few evolved and degassed MIs estimated to be entrapped at fO_2 < NNO − 0·2 (from 2006, 2008–2009 and 2013 products; Gennaro *et al.*, 2019). More generally, sulphide globules are rare in Etnean MIs and matrix glasses, and they always occur in evolved and degassed glasses (Spilliaert *et al.*, 2006*a*, 2006*b*; Collins *et al.*, 2009; Gennaro *et al.*, 2019). This rules out the segregation of important amounts of immiscible sulphide melt, despite the reduction experienced by the magma during crystallization. At fluid-saturated conditions, the most important effect of magma reduction is therefore to enhance S degassing, as sulphide species are significantly less soluble in the silicate melt than sulphate ones (Fig. 2a). Reduction-induced degassing is probably a more efficient mechanism than (1) a simple crystallization-driven degassing or (2) decompression, considering that the effect of fO_2 significantly enhances that of *P* in increasing the $DS^{fluid/melt}$ (Fig. 3). This process is therefore likely to account for the significant gas emissions observed at Mt Etna (e.g. McGonigle *et al.*, 2003; Aiuppa *et al.*, 2005, 2008; Salerno *et al.*, 2009; D'Aleo *et al.*, 2016; Delle Donne *et al.*, 2019).

CONCLUSIONS

S behaviour in basaltic magmas of Mt Etna (Italy) has been investigated by means of olivine-hosted melt inclusions and an experimental approach. The experimental study of S solubility in a hydrous basaltic melt from Mt Etna (Mt Spagnolo eruption) was performed at constant temperature and pressure (1200 °C and 200 MPa) and variable oxygen fugacity (NNO + 0·2 to NNO + 1·7). In addition to former studies, our results confirm the dependence of $DS^{fluid/melt}$ of the hydrous basaltic melt on the redox conditions, displaying a sulphur concentration of 6039 ± 232 ppm at NNO + 1·7 ± 0·5 with a $DS^{fluid/melt}$ of 51 ± 4.

Based on a selection of the obtained experimental $DS^{fluid/melt}$ values (50–146) and of those from the literature (1–209; e.g. Lesne *et al.*, 2011*a*; Zajacz *et al.*, 2013; Beermann *et al.*, 2015; Le Gall, 2015), an empirical model is proposed for basaltic melt composition to predict the variation of $DS^{fluid/melt}$ values upon variation of *P*, *T* and fO_2 conditions (25–300 MPa, 1030–1200 °C and between NNO − 0·8 and NNO + 2·4). This empirical model is applied to Mt Etna basaltic magmas, for which fO_2 conditions are here for the first time directly defined in olivine-hosted melt inclusions using XANES $Fe^{3+}/\Sigma Fe$ ratios.

Fe speciation in Etnean melt inclusions, together with olivine–spinel exchange (Ballhaus *et al.*, 1990, 1991) in the same products, reveals that the most

primitive FS (4 ka BP) and Mt Spagnolo (4–15 ka BP) magmas are highly oxidized (up to NNO + 1·6). The more evolved products from 2002–2013 eruptions indicate more reduced redox conditions, based on XANES $Fe^{3+}/\Sigma Fe$ ratios (NNO − 0·9 to NNO + 0·4) and Fe–Ti-spinel equilibria (NNO − 1·4 to NNO + 0·9). The S content of these Etnean MIs is extremely variable, from ~100 ppm to more than 4000 ppm.

Crystal fractionation and degassing models suggest that fractional crystallization coupled with magma degassing is the driving process accounting for both the variability in sulphur content and the large fO_2 variations observed in Etnean MIs.

The $DS^{fluid/melt}$ model coupled to the MELTS code (Ghiorso & Sack, 1995; Smith & Asimow, 2005) reveals that upon decrease of T and P, during fractional crystallization of ol + sp + cpx + plg (and volatile exsolution) of an FS-type magma, a significant fO_2 diminution occurs. The fO_2 reduction, in turn, causes a decrease in sulphur solubility and an increase in $DS^{fluid/melt}$. This increase becomes particularly important at $fO_2 \leq$ NNO + 1, when S is preferentially dissolved in the melt as S^{2-} (e.g. Carroll & Rutherford, 1985, 1987; Luhr, 1990; Jugo *et al.*, 2005), and $DS^{fluid/melt}$ is higher than 90, suggesting that S partitions favourably in the fluid phase.

Thus, important S degassing, as observed in the last decades at Mt Etna (McGonigle *et al.*, 2003; Aiuppa *et al.*, 2005, 2008; Salerno *et al.*, 2009; D'Aleo *et al.*, 2016; Delle Donne *et al.*, 2019), could highlight the ascent of magma batches, subjected to variation in fO_2 conditions associated to melt evolution.

ACKNOWLEDGEMENTS

We are grateful to I. Di Carlo (ISTO, Orléans) for her assistance with the SEM and the EMP, and to E. Deloule, J. Villeneuve and A. Gurenko (CRPG, Nancy) for their support during SIMS acquisitions. XANES analyses were carried out at the Diamond Light Source using beamline I18 (proposal number SP17250-1) with invaluable support received from K. Ignatyev. We thank A. Rizzo, A. Correale, M. Liotta and S. Rotolo (INGV, Palermo) for providing the Etnean samples, and for the precious discussions. We wish to thank O. Beermann, M. Masotta, two anonymous reviewers and the editor A. Audétat for their constructive reviews and useful comments.

FUNDING

This research has been financially supported by the Università degli Studi di Palermo, the Agence Campus France, the MEDiterranean SUpersite Volcanoes (MED-SUV) project, the 'Laboratoire d'Excellence VOLTAIRE' de l'Université d'Orléans, and the French Agence Nationale de la Recherche (ANR project #12-JS06-0009-01).

SUPPLEMENTARY DATA

Supplementary data are available at *Journal of Petrology* online.

REFERENCES

Aiuppa, A., Inguaggiato, S., McGonigle, A. J. S., O'dwyer, M., Oppenheimer, C., Padgett, M. J., Rouwet, D. & Valenza, M. (2005). H_2S fluxes from Mt. Etna, Stromboli, and Vulcano (Italy) and implications for the sulfur budget at volcanoes. *Geochimica et Cosmochimica Acta* **69**, 1861–1871.

Aiuppa, A., Giudice, G., Gurrieri, S., Liuzzo, M., Burton, M., Caltabiano, T., McGonigle, A. J. S., Salerno, G., Shinohara, H. & Valenza, M. (2008). Total volatile flux from Mount Etna. *Geophysical Research Letters* **35**, L24302, https://doi.org/10.1029/2008GL035871.

Allard, P., Behncke, B., D'Amico, S., Neri, M. & Gambino, S. (2006). Mount Etna 1993–2005: Anatomy of an evolving eruptive cycle. *Earth-Science Reviews* **78**, 85–114, https://doi.org/10.1016/j.earscirev.2006.04.002.

Alletti, M., Baker, D. R., Scaillet, B., Aiuppa, A., Moretti, R. & Ottolini, L. (2009). Chlorine partitioning between a basaltic melt and H_2O–CO_2 fluids at Mount Etna. *Chemical Geology* **263**, 37–50, https://doi.org/10.1016/j.chemgeo.2009.04.003.

Arató, R. & Audétat, A. (2017). FeTiMM—A new oxybarometer for mafic to felsic magmas. *Geochemical Perspectives Letters* **5**, 19–23, https://doi.org/10.7185/geochemlet.1740.

Armienti, P., Innocenti, F., Petrini, R., Pompilio, M. & Villari, L. (1988). Sub-aphyric alkali basalt from Mt. Etna: inferences on the depth and composition of the source magma. *Rendiconti della Società Italiana di Mineralogia e Petrologia* **43**, 877–891.

Armienti, P., Pareschi, M. T., Innocenti, F. & Pompilio, M. (1994). Effects of magma storage and ascent on the kinetics of crystal growth. *Contributions to Mineralogy and Petrology* **115**, 402–414.

Armienti, P., Tonarini, S., D'Orazio, M. & Innocenti, F. (2004). Genesis and evolution of Mt. Etna alkaline lavas: Petrological and Sr–Nd–B isotope constraints. *Periodico di Mineralogia* **73**, 29–52.

Armienti, P., Perinelli, C. & Putirka, K. D. (2013). A New Model to Estimate Deep-level Magma Ascent Rates, with Applications to Mt. Etna (Sicily, Italy). *Journal of Petrology* **54**, 795–813, https://doi.org/10.1093/petrology/egs085.

Ballhaus, C. (1993). Redox states of lithospheric and asthenospheric upper mantle. *Contributions to Mineralogy and Petrology* **114**, 331–348, https://doi.org/10.1007/BF01046536.

Ballhaus, C., Berry, R. F. & Green, D. H. (1990). Oxygen fugacity controls in the Earth's upper mantle. *Nature* **348**, 437–440, https://doi.org/10.1038/348437a0.

Ballhaus, C., Berry, R. F. & Green, D. H. (1991). High pressure experimental calibration of the olivine–orthopyroxene–spinel oxygen geobarometer: implications for the oxidation state of the upper mantle. *Contributions to Mineralogy and Petrology* **107**, 27–40, https://doi.org/10.1007/BF00311183.

Beermann, O., Botcharnikov, R., Holtz, F., Diedrich, O. & Nowak, M. (2011). Temperature dependence of sulfide and sulfate solubility in olivine-saturated basaltic magmas. *Geochimica et Cosmochimica Acta* **75**, 7612–7631, https://doi.org/10.1016/j.gca.2011.09.024.

Beermann, O., Botcharnikov, R. E. & Nowak, M. (2015). Partitioning of sulfur and chlorine between aqueous fluid and basaltic melt at 1050°C, 100 and 200 MPa. *Chemical Geology* **418**, 132–157, https://doi.org/10.1016/j.chemgeo.2015.08.008.

Beermann, O., Holtz, F. & Duesterhoeft, E. (2017). Magma storage conditions and differentiation of the mafic Lower Pollara volcanics, Salina Island, Aeolian Islands, Italy. *Contributions to Mineralogy and Petrology* **172**, 37, https://doi.org/10.1007/s00410-017-1363-z.

Binder, B. & Keppler, H. (2011). The oxidation state of sulfur in magmatic fluids. *Earth and Planetary Science Letters* **301**, 190–198, https://doi.org/10.1016/j.epsl.2010.10.042.

Binder, B., Wenzel, T. & Keppler, H. (2018). The partitioning of sulfur between multicomponent aqueous fluids and felsic melts. *Contributions to Mineralogy and Petrology* **173**, 18, https://doi.org/10.1007/s00410-018-1445-6.

Borisov, A. & McCammon, C. (2010). The effect of silica on ferric/ferrous ratio in silicate melts: An experimental study using Mossbauer spectroscopy. *American Mineralogist* **95**, 545–555, https://doi.org/10.2138/am.2010.3217.

Borisov, A., Behrens, H. & Holtz, F. (2015). Effects of melt composition on Fe^{3+}/Fe^{2+} in silicate melts: a step to model ferric/ferrous ratio in multicomponent systems. *Contributions to Mineralogy and Petrology* **169**, 24, https://doi.org/10.1007/s00410-015-1119-6.

Botcharnikov, R. E., Behrens, H., Holtz, F., Koepke, J. & Sato, H. (2004). Sulfur and chlorine solubility in Mt. Unzen rhyodacitic melt at 850°C and 200 MPa. *Chemical Geology* **213**, 207–225, https://doi.org/10.1016/j.chemgeo.2004.08.044.

Botcharnikov, R. E., Linnen, R. L., Wilke, M., Holtz, F., Jugo, P. J. & Berndt, J. (2011). High gold concentrations in sulphide-bearing magma under oxidizing conditions. *Nature Geoscience* **4**, 112–115.

Bourgue, E. & Richet, P. (2001). The effects of dissolved CO_2 on the density and viscosity of silicate melts: A preliminary study. *Earth and Planetary Science Letters* **193**, 57–68, https://doi.org/10.1016/S0012-821X(01)00491-5.

Branca, S., Coltelli, M. & Groppelli, G. (2011). Geological evolution of a complex basaltic stratovolcano: Mount Etna, Italy. *Italian Journal of Geosciences* **130**, 306–317, https://doi.org/10.3301/IJG.2011.13.

Brugier, Y. A., Alletti, M. & Pichavant, M. (2015). Fe pre-enrichment: A new method to counteract iron loss in experiments on basaltic melts. *American Mineralogist* **100**, 2106–2111, https://doi.org/10.2138/am-2015-5166.

Bucholz, C. E., Gaetani, G. A., Behn, M. D. & Shimizu, N. (2013). Post-entrapment modification of volatiles and oxygen fugacity in olivine-hosted melt inclusions. *Earth and Planetary Science Letters* **374**, 145–155, https://doi.org/10.1016/j.epsl.2013.05.033.

Burgisser, A. & Scaillet, B. (2007). Redox evolution of a degassing magma rising to the surface. *Nature* **445**, 194–197, https://doi.org/10.1038/nature05509.

Burnham, W. C. (1979). The Importance of Volatile Constituents. In: Yoder, H. S., Jr (ed.) *The Evolution of Igneous Rocks*. Princeton, NJ: Princeton University Press, pp. 439–482.

Carroll, M. R. & Rutherford, M. J. (1985). Sulfide and sulfate saturation in hydrous silicate melts. *Journal of Geophysical Research* **90**, C601–C612, https://doi.org/10.1029/JB090iS02p0C601.

Carroll, M. R. & Rutherford, M. J. (1987). The Stability of Igneous Anhydrite: Experimental Results and Implications for Sulfur Behavior in the 1982 El Chichon Trachyandesite and Other Evolved Magmas. *Journal of Petrology* **28**, 781–801, https://doi.org/10.1093/petrology/28.5.781.

Carroll, M. & Rutherford, M. (1988). Sulfur speciation in hydrous experimental glasses of varying oxidation-state—Results from measured wavelength shifts of sulfur X-rays. *American Mineralogist* **73**, 845–849.

Carroll, M. & Webster, J. D. (1994). Solubilities of sulfur, noble gases, nitrogen, chlorine and fluorine in magmas. Volatiles in Magmas 30. Mineralogical Society of America, Washington, pp. 231–279.

Cecchetti, A., Marianelli, P. & Sbrana, A. (2002). L'eruzione Di Astroni (Caldera Dei Campi Flegrei): Dati Preliminari Dallo Studio Di Inclusioni Silicatiche. *Atti della Società toscana di scienze naturali, Memorie, Serie A* **108**, 59–63.

Clemente, B., Scaillet, B. & Pichavant, M. (2004). The Solubility of Sulphur in Hydrous Rhyolitic Melts. *Journal of Petrology* **45**, 2171–2196, https://doi.org/10.1093/petrology/egh052.

Clocchiatti, R., Schiano, P., Ottolini, L. & Bottazzi, P. (1998). Earlier alkaline and transitional magmatic pulsation of Mt Etna volcano. *Earth and Planetary Science Letters* **163**, 399–407, https://doi.org/10.1016/S0012-821X(98)00170-8.

Cole-Dai, J., Ferris, D., Lanciki, A., Savarino, J., Baroni, M. & Thiemens, M. H. (2009). Cold decade (AD 1810–1819) caused by Tambora (1815) and another (1809) stratospheric volcanic eruption. *Geophysical Research Letters* **36**, 22, https://doi.org/10.1029/2009GL040882.

Collins, S. J., Pyle, D. M. & Maclennan, J. (2009). Melt inclusions track pre-eruption storage and dehydration of magmas at Etna. *Geology* **37**, 571–574, https://doi.org/10.1130/G30040A.1.

Coltelli, M., Del Carlo, P., Pompilio, M. & Vezzoli, L. (2005). Explosive eruption of a picrite: The 3930 BP subplinian eruption of Etna volcano (Italy). *Geophysical Research Letters* **32**, L23307, https://doi.org/10.1029/2005GL024271.

Correale, A., Paonita, A., Martelli, M., Rizzo, A., Rotolo, S. G., Corsaro, R. A. & Di Renzo, V. (2014). A two-component mantle source feeding Mt. Etna magmatism: Insights from the geochemistry of primitive magmas. *Lithos* **184–187**, 243–258, https://doi.org/10.1016/j.lithos.2013.10.038.

Corsaro, R. A. & Métrich, N. (2016). Chemical heterogeneity of Mt. Etna magmas in the last 15 ka. Inferences on their mantle sources. *Lithos* **252–253**, 123–134, https://doi.org/10.1016/j.lithos.2016.02.006.

Corsaro, R. A. & Pompilio, M. (2004). Buoyancy-controlled eruption of magmas at Mt Etna. *Terra Nova* **16**, 16–22, https://doi.org/10.1046/j.1365-3121.2003.00520.x.

Corsaro, R. A., Métrich, N., Allard, P., Andronico, D., Miraglia, L. & Fourmentraux, C. (2009). The 1974 flank eruption of Mount Etna: An archetype for deep dike-fed eruptions at basaltic volcanoes and a milestone in Etna's recent history. *Journal of Geophysical Research* **114**, B07204, https://doi.org/10.1029/2008JB006013.

Cottrell, E. & Kelley, K. A. (2011). The oxidation state of Fe in MORB glasses and the oxygen fugacity of the upper mantle. *Earth and Planetary Science Letters* **305**, 270–282, https://doi.org/10.1016/j.epsl.2011.03.014.

Cottrell, E., Kelley, K. A., Lanzirotti, A. & Fischer, R. A. (2009). High-precision determination of iron oxidation state in silicate glasses using XANES. *Chemical Geology* **268**, 167–179, https://doi.org/10.1016/j.chemgeo.2009.08.008.

D'Aleo, R., Bitetto, M., Delle Donne, D., Tamburello, G., Battaglia, A., Coltelli, M., Patanè, D., Prestifilippo, M., Sciotto, M. & Aiuppa, A. (2016). Spatially resolved SO_2 flux emissions from Mt Etna. *Geophysical Research Letters* **43**, 7511–7519, https://doi.org/10.1002/2016GL069938.

Danyushevsky, L. V. & Plechov, P. (2011). Petrolog3: Integrated software for modeling crystallization processes. *Geochemistry, Geophysics, Geosystems* **12, 7,** https://doi.org/10.1029/2011GC003516.

Danyushevsky, L. V., McNeill, A. W. & Sobolev, A. V. (2002). Experimental and petrological studies of melt inclusions in phenocrysts from mantle-derived magmas: an overview of techniques, advantages and complications. *Chemical*

Geology **183**, 5–24, https://doi.org/10.1016/S0009-2541(01)00369-2.

Delle Donne, D., Aiuppa, A., Bitetto, M., D'Aleo, R., Coltelli, M., Coppola, D., Pecora, E., Ripepe, M. & Tamburello, G. (2019). Changes in SO_2 Flux Regime at Mt. Etna Captured by Automatically Processed Ultraviolet Camera Data. *Remote Sensing* **11**, 1201, https://doi.org/10.3390/rs11101201.

Di Carlo, I., Pichavant, M., Rotolo, S. G. & Scaillet, B. (2006). Experimental Crystallization of a High-K Arc Basalt: the Golden Pumice, Stromboli Volcano (Italy). *Journal of Petrology* **47**, 1317–1343, https://doi.org/10.1093/petrology/egl011.

Di Renzo, V., Corsaro, R. A., Miraglia, L., Pompilio, M. & Civetta, L. (2019). Long and short-term magma differentiation at Mt. Etna as revealed by Sr–Nd isotopes and geochemical data. *Earth-Science Reviews* **190**, 112–130, https://doi.org/10.1016/j.earscirev.2018.12.008.

Dixon, J. E. & Pan, V. (1995). Determination of the molar absorptivity of dissolved carbonate in basanitic glass. *American Mineralogist* **80**, 1339–1342.

Dixon, J. E., Stolper, E. & Delaney, J. R. (1988). Infrared spectroscopic measurements of CO_2 and H_2O in Juan de Fuca Ridge basaltic glasses. *Earth and Planetary Science Letters* **90**, 87–104, https://doi.org/10.1016/0012-821X(88)90114-8.

Ferlito, C. & Lanzafame, G. (2010). The role of supercritical fluids in the potassium enrichment of magmas at Mount Etna volcano (Italy). *Lithos* **119**, 642–650.

Fiege, A., Holtz, F., Behrens, H., Mandeville, C. W., Shimizu, N., Crede, L. S. & Göttlicher, J. (2015). Experimental investigation of the S and S-isotope distribution between H_2O–S $\pm$ Cl fluids and basaltic melts during decompression. *Chemical Geology* **393–394**, 36–54, https://doi.org/10.1016/j.chemgeo.2014.11.012.

Fincham, C. J. B., Denys, R. F. & Frederick, G. C. (1954). The behaviour of sulphur in silicate and aluminate melts. *Proceedings of the Royal Society of London, Series A* **223**, 40–62, 10.1098/rspa.1954.0099.

Fortin, M.-A., Riddle, J., Desjardins-Langlais, Y. & Baker, D. R. (2015). The effect of water on the sulfur concentration at sulfide saturation (SCSS) in natural melts. *Geochimica et Cosmochimica Acta* **160**, 100–116, https://doi.org/10.1016/j.gca.2015.03.022.

Frezzotti, M.-L. (2001). Silicate-melt inclusions in magmatic rocks: applications to petrology. *Lithos* **55**, 273–299, https://doi.org/10.1016/S0024-4937(00)00048-7.

Frost, B. R. (1991). Introduction to oxygen fugacity and its petrologic importance. In: Lindsley, D. H. (ed.) Oxide Minerals: Petrologic and Magnetic Significance. *Washington, DC: Mineralogical Society of America, 508 pp. Reviews in Mineralogy,* 25, 1-9.

Gaetani, G. A. & Watson, E. B. (2000). Open system behavior of olivine-hosted melt inclusions. *Earth and Planetary Science Letters* **183**, 27–41, https://doi.org/10.1016/S0012-821X(00)00260-0.

Gaillard, F. & Scaillet, B. (2009). The sulfur content of volcanic gases on Mars. *Earth and Planetary Science Letters* **279**, 34–43, https://doi.org/10.1016/j.epsl.2008.12.028.

Gaillard, F., Scaillet, B. & Arndt, N. T. (2011). Atmospheric oxygenation caused by a change in volcanic degassing pressure. *Nature* **478**, 229–232, https://doi.org/10.1038/nature10460.

Gennaro, M. E. (2017). Sulfur behavior and redox conditions in Etnean hydrous basalts inferred from melt inclusions and experimental glasses. Ph.D. thesis, Université d'Orléans (France) and Università di Palermo (Italy).

Gennaro, E., Iacono-Marziano, G., Paonita, A., Rotolo, S. G., Martel, C., Rizzo, A. L., Pichavant, M. & Liotta, M. (2019). Melt inclusions track melt evolution and degassing of Etnean magmas in the last 15 ka. *Lithos* **324–325**, 716–732, https://doi.org/10.1016/j.lithos.2018.11.023.

Ghiorso, M. S. & Sack, R. O. (1995). Chemical mass transfer in magmatic processes IV. A revised and internally consistent thermodynamic model for the interpolation and extrapolation of liquid–solid equilibria in magmatic systems at elevated temperatures and pressures. *Contributions to Mineralogy and Petrology* **119**, 197–212, https://doi.org/10.1007/BF00307281.

Giacomoni, P. P., Coltorti, M., Bryce, J. G., Fahnestock, M. F. & Guitreau, M. (2016). Mt. Etna plumbing system revealed by combined textural, compositional, and thermobarometric studies in clinopyroxenes. *Contributions to Mineralogy and Petrology* **171**, 34, https://doi.org/10.1007/s00410-016-1247-7.

Guo, S., Bluth, G. J. S., Rose, W. I., Watson, I. M. & Prata, A. J. (2004). Re-evaluation of SO_2 release of the 15 June 1991 Pinatubo eruption using ultraviolet and infrared satellite sensors. *Geochemistry, Geophysics, Geosystems* **5, 4,** https://doi.org/10.1029/2003GC000654.

Hartley, M. E., Shorttle, O., Maclennan, J., Moussallam, Y. & Edmonds, M. (2017). Olivine-hosted melt inclusions as an archive of redox heterogeneity in magmatic systems. *Earth and Planetary Science Letters* **479**, 192–205, https://doi.org/10.1016/j.epsl.2017.09.029.

Holloway, J. R. (1987). Igneous fluids. In: Eugster, H. P. and Carmichael, I. S. E. (eds) Thermodynamic Modeling of Geological Materials: Minerals, Fluids and Melts, *Mineralogical Society of America. Reviews in Mineralogy* **17**, 211–233.

Humphreys, M. C. S., Brooker, R. A., Fraser, D. G., Burgisser, A., Mangan, M. T. & McCammon, C. (2015). Coupled interactions between volatile activity and Fe oxidation state during arc crustal processes. *Journal of Petrology* **56**, 795–814, https://doi.org/http://dx.doi.org/10.1093/petrology/egv017.

Iacono Marziano, G., Morizet, Y., Le Trong, E. & Gaillard, F. (2012). New experimental data and semi-empirical parameterization of H_2O–CO_2 solubility in mafic melts. *Geochimica et Cosmochimica Acta* **97**, 1–23, https://doi.org/10.1016/j.gca.2012.08.035.

Jochum, K. P., Stoll, B., Herwig, K., et al. (2006). MPI-DING reference glasses for *in situ* microanalysis: New reference values for element concentrations and isotope ratios. *Geochemistry, Geophysics, Geosystems* **7, 2,** https://doi.org/10.1029/2005GC001060.

Jugo, P. J. (2009). Sulfur content at sulfide saturation in oxidized magmas. *Geology* **37**, 415–418, https://doi.org/10.1130/G25527A.1.

Jugo, P. J., Luth, R. W. & Richards, J. P. (2005). An experimental study of the sulfur content in basaltic melts saturated with immiscible sulfide or sulfate liquids at 1300°C and 1·0 GPa. *Journal of Petrology* **46**, 783–798.

Kahl, M., Chakraborty, S., Costa, F. & Pompilio, M. (2011). Dynamic plumbing system beneath volcanoes revealed by kinetic modeling, and the connection to monitoring data: An example from Mt. Etna. *Earth and Planetary Science Letters* **308**, 11–22, https://doi.org/10.1016/j.epsl.2011.05.008.

Kahl, M., Chakraborty, S., Pompilio, M. & Costa, F. (2015). Constraints on the Nature and Evolution of the Magma Plumbing System of Mt. Etna Volcano (1991–2008) from a Combined Thermodynamic and Kinetic Modelling of the Compositional Record of Minerals. *Journal of Petrology* **56**, 2025–2068, https://doi.org/10.1093/petrology/egv063.

Kamenetsky, V. & Clocchiatti, R. (1996). Primitive magmatism of Mt. Etna: insights from mineralogy and melt inclusions.

Earth and Planetary Science Letters **142**, 553–572, https://doi.org/10.1016/0012-821X(96)00115-X.

Kamenetsky, V. S., Pompilio, M., Métrich, N., Sobolev, A. V., Kuzmin, D. V. & Thomas, R. (2007). Arrival of extremely volatile-rich high-Mg magmas changes explosivity of Mount Etna. *Geology* **35**, 255–258, https://doi.org/10.1130/G23163A.1.

Kelley, K. A. & Cottrell, E. (2012). The influence of magmatic differentiation on the oxidation state of Fe in a basaltic arc magma. *Earth and Planetary Science Letters* **329–330**, 109–121, https://doi.org/10.1016/j.epsl.2012.02.010.

Kress, V. C. & Carmichael, I. S. E. (1991). The compressibility of silicate liquids containing Fe_2O_3 and the effect of composition, temperature, oxygen fugacity and pressure on their redox states. *Contributions to Mineralogy and Petrology* **108**, 82–92, https://doi.org/10.1007/BF00307328.

Le Gall, N. (2015). Ascension et dégazage des magmas basaltiques: approche expérimentale. Ph.D. thesis, Université d'Orléans.

Lesne, P. (2008). Etude expérimentale de la solubilité des volatils C–H–O–S dans les basaltes alcalins italiens. Simulations numériques du dégazage chimique: application à l'Etna. Ph.D. thesis, Université d'Orléans.

Lesne, P., Kohn, S. C., Blundy, J., Witham, F., Botcharnikov, R. E. & Behrens, H. (2011a). Experimental Simulation of Closed-System Degassing in the System Basalt–H_2O–CO_2–S–Cl. *Journal of Petrology* **52**, 1737–1762, https://doi.org/10.1093/petrology/egr027.

Lesne, P., Scaillet, B., Pichavant, M. & Bény, J.-M. (2011b). The carbon dioxide solubility in alkali basalts: an experimental study. *Contributions to Mineralogy and Petrology* **162**, 153–168, https://doi.org/10.1007/s00410-010-0585-0.

Lesne, P., Scaillet, B. & Pichavant, M. (2015). The solubility of sulfur in hydrous basaltic melts. *Chemical Geology* **418**, 104–116, https://doi.org/10.1016/j.chemgeo.2015.03.025.

Li, C. & Ripley, E. M. (2009). Sulfur Contents at Sulfide–Liquid or Anhydrite Saturation in Silicate Melts: Empirical Equations and Example Applications. *Economic Geology* **104**, 405–412, https://doi.org/10.2113/gsecongeo.104.3.405.

Liu, Y., Samaha, N.-T. & Baker, D. R. (2007). Sulfur concentration at sulfide saturation (SCSS) in magmatic silicate melts. *Geochimica et Cosmochimica Acta* **71**, 1783–1799, https://doi.org/10.1016/j.gca.2007.01.004.

Luhr, J. F. (1990). Experimental Phase Relations of Water- and Sulfur-Saturated Arc Magmas and the 1982 Eruptions of El Chichón Volcano. *Journal of Petrology* **31**, 1071–1114, https://doi.org/10.1093/petrology/31.5.1071.

Masotta, M. & Keppler, H. (2015). Anhydrite solubility in differentiated arc magmas. *Geochimica et Cosmochimica Acta* **158**, 79–102, https://doi.org/10.1016/j.gca.2015.02.033.

Masotta, M., Keppler, H. & Chaudhari, A. (2016). Fluid–melt partitioning of sulfur in differentiated arc magmas and the sulfur yield of explosive volcanic eruptions. *Geochimica et Cosmochimica Acta* **176**, 26–43, https://doi.org/10.1016/j.gca.2015.12.014.

Mathez, E. A. (1984). Influence of degassing on oxidation states of basaltic magmas. *Nature* **310**, 371–375, https://doi.org/10.1038/310371a0.

McGonigle, A. J. S., Oppenheimer, C., Hayes, A. R., Galle, B., Edmonds, M., Caltabiano, T., Salerno, G., Burton, M. & Mather, T. A. (2003). Sulphur dioxide fluxes from Mount Etna, Vulcano, and Stromboli measured with an automated scanning ultraviolet spectrometer. *Journal of Geophysical Research: Solid Earth* **108**, 2455, https://doi.org/10.1029/2002JB002261.

Métrich, N. & Clocchiatti, R. (1989). Melt inclusion investigation of the volatile behaviour in historic alkali basaltic magmas of Etna. *Bulletin of Volcanology* **51**, 185–198, https://doi.org/10.1007/BF01067955.

Métrich, N. & Clocchiatti, R. (1996). Sulfur abundance and its speciation in oxidized alkaline melts. *Geochimica et Cosmochimica Acta* **60**, 4151–4160, https://doi.org/10.1016/S0016-7037(96)00229-3.

Métrich, N. & Rutherford, M. J. (1998). Low Pressure Crystallization Paths of H_2O-Saturated Basaltic–Hawaiitic Melts from Mt Etna: Implications for Open-System Degassing of Basaltic Volcanoes. *Geochimica et Cosmochimica Acta* **62**, 1195–1205, https://doi.org/10.1016/S0016-7037(98)00048-9.

Métrich, N., Allard, P., Spilliaert, N., Andronico, D. & Burton, M. (2004). 2001 flank eruption of the alkali- and volatile-rich primitive basalt responsible for Mount Etna's evolution in the last three decades. *Earth and Planetary Science Letters* **228**, 1–17, https://doi.org/10.1016/j.epsl.2004.09.036.

Métrich, N., Berry, A. J., O'Neill, H. S. C. & Susini, J. (2009). The oxidation state of sulfur in synthetic and natural glasses determined by X-ray absorption spectroscopy. *Geochimica et Cosmochimica Acta* **73**, 2382–2399, https://doi.org/10.1016/j.gca.2009.01.025.

Mollo, S., Giacomoni, P. P., Coltorti, M., Ferlito, C., Iezzi, G. & Scarlato, P. (2015). Reconstruction of magmatic variables governing recent Etnean eruptions: Constraints from mineral chemistry and P–T–fO_2–H_2O modeling. *Lithos* **212–215**, 311–320, https://doi.org/10.1016/j.lithos.2014.11.020.

Moore, L. R., Gazel, E., Tuohy, R., Lloyd, A. S., Esposito, R., Steele-MacInnis, M., Hauri, E. H., Wallace, P. J., Plank, T. & Bodnar, R. J. (2015). Bubbles matter: An assessment of the contribution of vapor bubbles to melt inclusion volatile budgets. *American Mineralogist* **100**, 806–823, https://doi.org/10.2138/am-2015-5036.

Moretti, R. & Baker, D. R. (2008). Modeling the interplay of fO_2 and fS_2 along the FeS–silicate melt equilibrium. *Chemical Geology* **256**, 286–298, https://doi.org/10.1016/j.chemgeo.2008.06.055.

Moretti, R., Métrich, N., Arienzo, I., Di Renzo, V., Aiuppa, A. & Allard, P. (2018). Degassing vs. eruptive styles at Mt. Etna volcano (Sicily, Italy). Part I: Volatile stocking, gas fluxing, and the shift from low-energy to highly explosive basaltic eruptions. *Chemical Geology* **482**, 1–17, https://doi.org/10.1016/j.chemgeo.2017.09.017.

Morizet, Y., Gennaro, E., Jego, S., Zajacz, Z., Iacono-Marziano, G., Pichavant, M., Carlo, I. D., Ferraina, C. & Lesne, P. (2017). A Raman calibration for the quantification of SO_4^{2-} groups dissolved in silicate glasses: Application to natural melt inclusions. *American Mineralogist* **102**, 2065–2076, https://doi.org/10.2138/am-2017-6100.

Moune, S., Holtz, F. & Botcharnikov, R. E. (2009). Sulphur solubility in andesitic to basaltic melts: implications for Hekla volcano. *Contributions to Mineralogy and Petrology* **157**, 691–707, https://doi.org/10.1007/s00410-008-0359-0.

Moussallam, Y., Oppenheimer, C., Scaillet, B., Gaillard, F., Kyle, P., Peters, N., Hartley, M., Berlo, K. & Donovan, A. (2014). Tracking the changing oxidation state of Erebus magmas, from mantle to surface, driven by magma ascent and degassing. *Earth and Planetary Science Letters* **393**, 200–209, https://doi.org/10.1016/j.epsl.2014.02.055.

Moussallam, Y., Edmonds, M., Scaillet, B., Peters, N., Gennaro, E., Sides, I. & Oppenheimer, C. (2016). The impact of degassing on the oxidation state of basaltic magmas: A case study of Kīlauea volcano. *Earth and Planetary Science Letters* **450**, 317–325, https://doi.org/10.1016/j.epsl.2016.06.031.

Moussallam, Y., Longpré, M.-A., McCammon, C., Gomez-Ulla, A., Rose-Koga, E. F., Scaillet, B., Peters, N., Gennaro, E., Paris, R. & Oppenheimer, C. (2019). Mantle plumes are oxidised. *Earth and Planetary Science Letters* **527**, 115798, https://doi.org/10.1016/j.epsl.2019.115798.

O'Neill, H. S. C., Berry, A. J. & Mallmann, G. (2018). The oxidation state of iron in Mid-Ocean Ridge Basaltic (MORB) glasses: Implications for their petrogenesis and oxygen fugacities. *Earth and Planetary Science Letters* **504**, 152–162, https://doi.org/10.1016/j.epsl.2018.10.002.

Oppenheimer, C. (2003). Volcanic Degassing. In: *Treatise on Geochemistry* **3**, 123–166. Editor: R. L. Rudnick, Executive Editors: H. D. Holland and K. K. Turekian. pp. 659, Elsevier. https://doi.org/10.1016/B0-08-043751-6/03020-6.

Parkinson, I. & Arculus, R. J. (1999). Redox state of subduction zones: insights from arc-peridotites. *Chemical Geology* **160**, 409–423.

Pichavant, M., Scaillet, B., Di Carlo, I., Rotolo, S. & Métrich, N. (2006). Sulfur in hydrous, oxidized basaltic magmas: phase equilibria and melt solubilities. Presented at the American Geophysical Union (AGU) 2006 joint assembly, Baltimora. *EOS Transactions, American Geophysical Union, pp.* 1–2.

Pichavant, M., Scaillet, B., Pommier, A., Iacono-Marziano, G. & Cioni, R. (2014). Nature and Evolution of Primitive Vesuvius Magmas: an Experimental Study. *Journal of Petrology* **55**, 2281–2310, https://doi.org/10.1093/petrology/egu057.

Pownceby, M. I. & O'Neill, H. S. C. (1994). Thermodynamic data from redox reactions at high temperatures. IV. Calibration of the Re–ReO_2 oxygen buffer from EMF and NiO + Ni–Pd redox sensor measurements. *Contributions to Mineralogy and Petrology* **118**, 130–137, https://doi.org/10.1007/BF01052864.

Richet, P., Whittington, A., Holtz, F., Behrens, H., Ohlhorst, S. & Wilke, M. (2000). Water and the density of silicate glasses. *Contributions to Mineralogy and Petrology* **138**, 337–347, https://doi.org/10.1007/s004100050567.

Robidoux, P., Aiuppa, A., Rotolo, S. G., Rizzo, A. L., Hauri, E. H. & Frezzotti, M. L. (2017). Volatile contents of mafic-to-intermediate magmas at San Cristóbal volcano in Nicaragua. *Lithos* **272–273**, 147–163.

Robie, R. A., Hemingway, B. S. & Fisher, J. R. (1979). Thermodynamic properties of minerals and related substances at 298·15 K and 1 bar (105 pascals) pressure and at higher temperatures. US Geological Survey Bulletin 1452, 456.

Robock, A. (2000). Volcanic eruptions and climate. *Reviews of Geophysics* **38**, 191–219, https://doi.org/10.1029/1998RG000054.

Salem, L. C., Edmonds, M., Corsaro, R. A. & Maclennan, J. (2019). Carbon dioxide in geochemically heterogeneous melt inclusions from Mount Etna. *Geochemistry, Geophysics, Geosystems* **20**, 3150–3169, https://agupubs.onlinelibrary.wiley.com/doi/abs/10.1029/2018GC008027.

Salerno, G. G., Burton, M. R., Oppenheimer, C., Caltabiano, T., Randazzo, D., Bruno, N. & Longo, V. (2009). Three years of SO_2 flux measurements of Mt. Etna using an automated UV scanner array: Comparison with conventional traverses and uncertainties in flux retrieval. *Journal of Volcanology and Geothermal Research* **183**, 76–83, https://doi.org/10.1016/j.jvolgeores.2009.02.013.

Schiano, P. & Clocchiatti, R. (1994). Worldwide occurrence of silica-rich melts in sub-continental and sub-oceanic mantle minerals. *Nature* **368**, 621–624, https://doi.org/10.1038/368621a0.

Schiavi, F., Rosciglione, A., Kitagawa, H., Kobayashi, K., Nakamura, E., Nuccio, P. M., Ottolini, L., Paonita, A. & Vannucci, R. (2015). Geochemical heterogeneities in magma beneath Mount Etna recorded by 2001–2006 melt inclusions. *Geochemistry, Geophysics, Geosystems* **16**, 2109–2126, https://doi.org/10.1002/2015GC005786.

Shishkina, T. A., Botcharnikov, R. E., Holtz, F., Almeev, R. R. & Portnyagin, M. V. (2010). Solubility of H2O- and CO2-bearing fluids in tholeiitic basalts at pressures up to 500 MPa. *Chemical Geology* **277**, 115–125, https://doi.org/10.1016/j.chemgeo.2010.07.014.

Smith, P. M. & Asimow, P. D. (2005). Adiabat_1ph: A new public front-end to the MELTS, pMELTS, and pHMELTS models. *Geochemistry, Geophysics, Geosystems* **6**, Q02004, https://doi.org/10.1029/2004GC000816.

Spilliaert, N., Allard, P., Métrich, N. & Sobolev, A. V. (2006a). Melt inclusion record of the conditions of ascent, degassing, and extrusion of volatile-rich alkali basalt during the powerful 2002 flank eruption of Mount Etna (Italy). *Journal of Geophysical Research* **111**, B04203, https://doi.org/10.1029/2005JB003934.

Spilliaert, N., Métrich, N. & Allard, P. (2006b). S–Cl–F degassing pattern of water-rich alkali basalt: Modelling and relationship with eruption styles on Mount Etna volcano. *Earth and Planetary Science Letters* **248**, 772–786, https://doi.org/10.1016/j.epsl.2006.06.031.

Stolper, E. (1982). Water in silicate glasses: An infrared spectroscopic study. *Contributions to Mineralogy and Petrology* **81**, 1–17, https://doi.org/10.1007/BF00371154.

Taylor, J. R., Wall, V. J. & Pownceby, M. I. (1992). The calibration and application of accurate redox sensors. *American Mineralogist* **77**, 284–295.

Thordarson, T. & Self, S. (2003). Atmospheric and environmental effects of the 1783–1784 Laki eruption: A review and reassessment. *Journal of Geophysical Research* **108**, AAC 7-1–AAC 7-29, https://doi.org/10.1029/2001JD002042.

Trigila, R., Spera, F. J. & Aurisicchio, C. (1990). The 1983 Mount Etna eruption: thermochemical and dynamical inferences. *Contributions to Mineralogy and Petrology* **104**, 594–608, https://doi.org/10.1007/BF00306667.

Viccaro, M., Giacomoni, P. P., Ferlito, C. & Cristofolini, R. (2010). Dynamics of magma supply at Mt. Etna volcano (Southern Italy) as revealed by textural and compositional features of plagioclase phenocrysts. *Lithos* **116**, 77–91, https://doi.org/10.1016/j.lithos.2009.12.012.

Von Aulock, F. W., Kennedy, B. M., Schipper, C. I., Castro, J. M., Martin, D. E., Oze, C., Watkins, J. M., Wallace, P. J., Puskar, L., Bégué, F., Nichols, A. R. L. & Tuffen, H. (2014). Advances in Fourier transform infrared spectroscopy of natural glasses: From sample preparation to data analysis. *Lithos* **206–207**, 52–64.

Vidal, C. M., Métrich, N., Komorowski, J.-C., Pratomo, I., Michel, A., Kartadinata, N., Robert, V. & Lavigne, F. (2016). The 1257 Samalas eruption (Lombok, Indonesia): the single greatest stratospheric gas release of the Common Era. *Scientific Reports* **6**, 34868, https://doi.org/10.1038/srep34868.

Wallace, P. J. & Carmichael, I. S. E. (1994). S speciation in submarine basaltic glasses as determined by measurements of SKα X-ray wavelength shifts. *American Mineralogist* **79**, 161–167.

Wallace, P. J. & Edmonds, M. (2011). The Sulfur Budget in Magmas: Evidence from Melt Inclusions, Submarine Glasses, and Volcanic Gas Emissions. In: Behrens, H. and Webster, J. D. (eds) Sulfur in Magmas and Melts: Its Importance for Natural and Technical Processes246, Mineralogical Society of America and Geochemical Society. Reviews in Mineralogy and Geochemistry, https://doi.org/10.2138/rmg.2011.73.8.

Wallace, P. J., Plank, T., Edmonds, M. & Hauri, E. H. (2015). Volatiles in Magmas. In: Sigurdsson, H. (ed.) *Encyclopedia of Volcanoes*, 2nd edn. Amsterdam: Elsevier, pp. 163–183.

Waters, L. E. & Lange, R. A. (2016). No effect of H_2O degassing on the oxidation state of magmatic liquids. *Earth and Planetary Science Letters* **447**, 48–59, https://doi.org/10.1016/j.epsl.2016.04.030.

Webster, J. D. & Botcharnikov, R. E. (2011). Distribution of Sulfur Between Melt and Fluid in S–O–H–C–Cl-Bearing Magmatic Systems at Shallow Crustal Pressures and Temperatures. In: Behrens, H. and Webster, J. D. (eds) Sulfur in Magmas and Melts: Its Importance for Natural and Technical Processes, *Mineralogical Society of America and Geochemical Society. Reviews in Mineralogy and Geochemistry 73, 247–283,*https://doi.org/10.2138/rmg.2011.73.9.

Wilke, M., Behrens, H., Burkhard, D. J. M. & Rossano, S. (2002). The oxidation state of iron in silicic melt at 500 MPa water pressure. *Chemical Geology* **189**, 55–67, 10.1016/S0009-2541(02)00042-6.

Zajacz, Z., Candela, P. A., Piccoli, P. M. & Sanchez-Valle, C. (2012). The partitioning of sulfur and chlorine between andesite melts and magmatic volatiles and the exchange coefficients of major cations. *Geochimica et Cosmochimica Acta* **89**, 81–101, https://doi.org/10.1016/j.gca.2012.04.039.

Zajacz, Z., Candela, P. A., Piccoli, P. M., Sanchez-Valle, C. & Wälle, M. (2013). Solubility and partitioning behavior of Au, Cu, Ag and reduced S in magmas. *Geochimica et Cosmochimica Acta* **112**, 288–304, https://doi.org/10.1016/j.gca.2013.02.026.

Zhang, H. L., Cottrell, E., Solheid, P. A., Kelley, K. A. & Hirschmann, M. M. (2018). Determination of $Fe^{3+}/\Sigma Fe$ of XANES basaltic glass standards by Mössbauer spectroscopy and its application to the oxidation state of iron in MORB. *Chemical Geology* **479**, 166–175, https://doi.org/10.1016/j.chemgeo.2018.01.006.